LASER SPECTROSCOPY STUDIES OF ENERGY TRANSFER IN $YVO_4:Eu^{3+}$, Er^{3+}

By

GEORGE VENIKOUAS

Bachelor

University of Thessaloniki

Thessaloniki, Greece

1970

Submitted to the Faculty of the Graduate College
of the Oklahoma State University
in partial fulfillment of the requirements
for the Degree of
DOCTOR OF PHILOSOPHY
May, 1978

LASER SPECTROSCOPY STUDIES OF ENERGY TRANSFER IN YVO_4:Eu^{3+}, Er^{3+}

Thesis Approved:

Richard C. Powell
Thesis Adviser

W. A. Sibley

Joel J. Martin

A. L. Rockley

Norman N. Durham
Dean of the Graduate College

ACKNOWLEDGMENTS

I would like to express my appreciation to all the people responsible for the completion of this thesis. First, my special thanks to my adviser, Professor R. C. Powell, for his help and direction throughout this research work. Second, I am deeply appreciative of the patience and understanding of my wife during this time of hard work and late hours. Third, I would like to acknowledge my appreciation to Dolores Behrens for her expert typing of this manuscript and all her help above and beyond the call of duty. Finally, I acknowledge the support of the U. S. Army Research Office who sponsored this research project.

TABLE OF CONTENTS

Chapter		Page
I.	INTRODUCTION	1
	Theoretical Background	2
	Large Energy Mismatch	10
	Small Energy Mismatch	12
	Nonresonant-Phonon-Assisted Energy Transfer Within the First Excited Level: One Phonon	14
	Nonresonant-Phonon-Assisted Energy Transfer Within the First Excited Level: Two Phonon	18
	Resonant Phonon-Assisted Energy Transfer Via the Second Excited Level	21
	Nonresonant-Phonon-Assisted Energy Transfer Via the Second Excited Level	29
	Apparatus	32
	Lifetime Measurements	35
	Time Resolved Spectroscopy Measurements	36
	Absorption and Excitation Measurements	36
II.	HOST-SENSITIZED ENERGY TRANSFER IN Eu^{3+} AND Er^{3+} DOPED YVO_4	39
	Introduction	39
	Results and Interpretation of Undoped YVO_4 Data	40
	Results and Interpretation of YVO_4:Eu^{3+} Data	45
	Results and Interpretation of YVO_4:Er^{3+} Data	54
	Discussion	67
III.	LASER SITE SELECTION INVESTIGATION OF Eu^{3+} IONS IN YVO_4 CRYSTALS	73
	Introduction	74
	Experimental	75
	Samples and Equipment	75
	Results	76
	Interpretation	79
	Discussion	89

Chapter | Page

IV. SUMMARY AND CONCLUSIONS. 93

The Host-Sensitized YVO_4Eu^{3+} and $YVO_4:Er^{3+}$ Systems 94
Site Selection Spectroscopy of Eu^{3+} in $YVO_4:Eu^{3+}$ 95
Conclusions 96

REFERENCES 96

LIST OF TABLES

Table		Page
I.	Model Fitting Parameters	44
II.	Fluorescence Lifetimes and Risetime for $YVO_4:Eu^{3+}$ System	47
III.	Fluorescence Intensity Ratios at Different Times After the Laser Pulse	49
IV.	Lifetimes and Risetimes of the System $YVO_4:Er^{3+}$ at Different Temperatures	59
V.	Fluorescence Intensities and Lifetime Ratios of $YVO_4:Er^{3+}$ at Different Temperatures	62
VI.	Fluorescence Intensity Ratios at Different Times After the Laser Pulse at Room Temperature in $YVO_4:Er^{3+}$	64
VII.	Exciton Migration and Trapping Parameters	70
VIII.	Decay Times of the Three Eu^{3+} Emission Lines	78
IX.	Fluorescence Intensity Ratios for High Energy Excitation Measured at Different Times After Pulse (Figure 19)	81

LIST OF FIGURES

Figure		Page
1.	Schematic Diagram Indicating Ground and Excited States of Two Sites and Various Mechanisms of One and Two Phonon Processes Amont These Two Sites.	6
2.	Schematic Diagram Indicating Ground and Excited States of Two Sites and Various Mechanisms of One and Two Phonon Processes Among These Two Sites.	16
3.	Schematic Diagram Indicating Ground and Excited States of Two Sites and Various Mechanisms of One and Two Phonon Processes Among These Two Sites.	19
4a.	Schematic Diagram Indicating Ground and Excited States of Two Sites and Various Mechanisms of One and Two Phonon Processes Among These Two Sites.	22
4b.	Schematic Diagram Indicating Ground and Excited States of Two Sites and Various Mechanisms of One and Two Phonon Processes Among These Two Sites.	24
4c.	Schematic Diagram Indicating Ground and Excited States of Two Sites and Various Mechanisms of One and Two Phonon Processes Among These Two Sites.	25
5.	Time Resolved Spectroscopy Apparatus.	33
6.	Block Diagram of the Continuous Fluorescence Measurement Apparatus Used for Obtaining Excitation Spectra	37
7.	Zircon Structure of YVO_4.	41
8.	Temperature Dependences of the Fluorescence Decay Times and Rise Times of Undoped YVO_4 Crystals with 3371Å Laser Excitation; the Solid Line is from Eq. (2-1). . . .	42
9.	Temperature Dependences of the Fluorescence Decay Times in $YVO_4:Eu^{3+}$; Eu_0 and Eu_1 Indicate Emission from the $^5D_0$ and $^5D_1$ States, Respectively.	46
10.	Laser TRS Results for $YVO_4:Eu^{3+}$ Crystals with 1.27×10^{19} cm^{-3} Eu^{3+}; See Text for Explanation of Theoretical Lines	48

Figure Page

11. Model for Host-Sensitized Energy Transfer in $YVO_4:Eu^{3+}$ 51

12. Room Temperature Absorption Spectrum of $YVO_4:Er^{3+}$ Crystal with 1.27×10^{20} cm^{-3} Er^{3+}; Sample Thickness is 0.9 mm 55

13a. Fluorescence Spectrum of $YVO_4:Er^{3+}$ with 1.27×10^{20} cm^{-3} Er^{3+} Taken at Room Temperature 56

13b. Fluorescence Spectrum of $YVO_4:Er^{3+}$ with 1.27×10^{20} cm^{-3} Er^{3+} Taken at $13^{o}K$ 57

14. Temperature Dependences of the Fluorescence Decay Times in $YVO_4:Er^{3+}$; Er_0 and Er_1 Indicate Emission from the $^4S_{3/2}$ and $^2H_{11/2}$ States, Respectively. 58

15. Temperature Dependences of the Fluorescence Intensity and Lifetime Ratios in $YVO_4:Er^{3+}$; I_T Represents the Sum of All the Er^{3+} Transitions; the Intensities are Measured at 0.7 μs After the Laser Pulse; the Solid Lines are Given by Exp [1,000 $cm^{-1}/(k_BT)$] 61

16. Laser TRS Results for $YVO_4:Er^{3+}$ Crystals with 1.27×10^{20} cm^{-3} Er^{3+} 63

17. Model for Host-Sensitized Energy Transfer in $YVO_4:Er^{3+}$. . . 65

18. Absorption Line of the $^7F_0$-$^5D_2$ Transition of $YVO_4:Eu^{3+}$; Pumping at the High (H.E.) and Low (L.E.) Energy Side of This Line Produced Fluorescence Depicted on the Upper Two Scaled Down Diagrams. 77

19. Ratios of the Intensities of the High (I_H) and Low (I_L) Energy Emission Lines to That of the Middle Line as a Function of Time After the Laser Pulse for 4667.8Å Excitation at $11^{o}K$. 80

20. Ratios of the Intensities of High (I_H), Middle (I_M) and Low (I_L) Energy Emission Lines, to the Sum of the Three Intensities as a Function of Time After the Laser Pulse for 4669.0Å Excitation at $11^{o}K$. 82

21. Temperature Dependence of the Intensity Ratios Taken at 25 and 500 μs After the Laser Pulse. 83

22. Model Used for Interpreting the Site Selection Spectroscopy Results for $YVO_4:Eu^{3+}$ 84

CHAPTER I

INTRODUCTION

Rare earth ions in solids have found important applications as lasers, phosphors, quantum counters and frequency upconverters. Energy migration is a fundamental physical process of great importance in all of these applications. The use of fast pulsed lasers has made time resolved spectroscopy (TRS) a powerful new technique for characterizing the properties of energy transfer. Also, by using high resolution tunable dye lasers it is now possible to probe ion-ion interaction on a detailed microscopic scale never before possible. This is called "site selection spectroscopy."

Yttrium vanadate is an important material as a laser host, a color television and lamp phosphor and an infrared polarizer. In this study, investigations concerning energy migration were made of trivalent europium and erbium ions in yttrium vanadate crystals in an effort to obtain a better understanding of the mechanism that governs this migration. There are two parts in this investigation. The first is host sensitized energy transfer in yttrium vanadate crystals doped with europium and erbium. The second part is site selection spectroscopy of europium in yttrium vanadate using narrow band laser excitation techniques.

In the first part, the absorption and excitation spectra are obtained, as well as lifetime measurements, as a function of temperature

and fluorescence spectra as a function of time (time resolved spectroscopy) and temperature. The host sensitized energy transfer is explained by models based on either single step electric dipole-dipole interaction process from self-trapped excitons, or thermally activated exciton hopping, with activator induced host traps being important in the trapping process. In the latter case exchange interaction was considered for both hopping and trapping steps.

In the second part, a narrow band laser is used to excite europium ions. The fluorescence emission indicates the presence of several different types of crystal field sites. Two different sites are selectively excited and time dependent fluorescence spectra as well as lifetimes are obtained at different temperatures. A model is used to explain the energy transfer based on resonant electric-dipole-dipole interaction and it appears that the europium ions have a tendency to form clusters.

Theoretical Background

In the study of energy migration we are interested in two different types of atoms. The first is the atom that absorbs the excitation energy and we call it the "sensitizer" and the second is the atom that emits the energy and we call it the "activator."

The energy migration among ions in solids can be divided into three general categories:

1. Single Step
2. Diffusion Limited
3. Fast Diffusion.

A general expression for the time evolution of the excitation $\rho(\vec{R}_s,t)$

of the sensitizer is:

$$\frac{\partial \rho(\vec{R}_s,t)}{\partial t} = -\frac{1}{\tau_s^o}\rho(\vec{R}_s,t) + D\nabla^2\rho(\vec{R}_s,t) - \sum_{i=1}^{N} W_{sa}(\vec{R}_s-\vec{R}_{a_i})\rho(\vec{R}_s,t) \qquad (1\text{-}1)$$

The first term represents the internal dissipation of energy through radiative or radiationless transitions with a rate $(\tau_s^o)^{-1}$. The second term accounts for the migration of energy to other sensitizer sites with a diffusion coefficient D. The third term describes the transfer to an activator site at $\vec{R}_{a_i}$ with a rate $W_{sa}(\vec{R}_s-\vec{R}_{a_i})$. Here it has been assumed that all sensitizer atoms are in resonance, which is valid only if there is no inhomogeneous broadening present. Since the activator environment of each excited sensitizer ion is different, we take the statistical average over the ionic distribution.

$$\Phi_s(t) = \int \rho(\vec{R}_s,t)d^3\vec{R}_s \qquad (1\text{-}2)$$

where $\Phi_s(t)$ describes the time evolution of the fluorescence intensity of the sensitizer.

In the low sensitizer concentration limit the interaction between sensitizer ions is negligible and the second term of Eq. (1-1) vanishes, so that single step energy transfer takes place, from excited sensitizer to randomly distributed activator ions. The solution of Eq. (1-2) in the case of electric-multipole interaction is given by:

$$\Phi_s(t) = \Phi_s(o)\exp\left[-\frac{t}{\tau_s^o} - \Gamma\left(1-\frac{3}{q}\right)\left(\frac{C}{C_o}\right)\left(\frac{t}{\tau_s^o}\right)^{3/q}\right] \qquad (1\text{-}3)$$

where q is equal to 6, 8, 10 for electric-dipole-dipole (EDD),

electric-dipole-quadropole (EDQ) and electric-quadropole-quadropole (EQQ) interaction respectively. C_o is called "critical concentration" and is given by:

$$C_o = \frac{3}{4\pi R_o^3} \qquad (1\text{-}4)$$

$$R_o = \left[5.86 \times 10^{-25} (\Omega \eta_s^o)/(n\bar{\nu}_{sa})^4 \right]^{1/6}$$

where R_o is the so called "critical interaction distance," Ω is the "spectral overlap integral," in units of liters $mole^{-1}cm^{-1}$, η_s^o is the "quantum efficiency" of the sensitizer, n is the index of refraction and $\bar{\nu}_{sa}$ is the average wave number of the spectral overlap. The expressions (1-3) and (1-4) become more complicated for magnetic and exchange interactions.

In the case of high concentrations of sensitizers the interaction among them is no longer negligible. The process can be pictured as localized (Frenkel) exciton hopping incoherently from one random site to the next. In the limit of very high concentrations, the third term of Eq. (1-1) becomes negligible. Theoretical treatment at the true exciton case gave an energy transfer rate

$$W_D = 4\pi DRC_a \qquad (1\text{-}5)$$

$$\ell = \sqrt{2D\tau_s^o} \qquad (1\text{-}6)$$

$$t_h = \bar{R}_{ss}^2/(6D) \qquad (1\text{-}7)$$

$$N = \tau_s^o/t_h \qquad (1\text{-}8)$$

where W_D is the energy transfer rate, D is the "diffusion coefficient," ℓ is the "diffusion length," t_h is the average hopping time, and N is

the number of steps in the random walk. Each step is described as an electromagnetic multipole or exchange process. The "diffusion limited" case has been solved only for the case of EDD with very complicated results (1).

Up to now a summary of various forms of energy transfer has been given since these forms are extensively studied and publicized. A very interesting case that is not characterized well and is going to be examined here in a little more detailed way is the one and two phonon assisted energy transfer that has been developed by R. Orbach and coworkers (2,3).

Let us consider the diagram of Figure 1. Designating the electronic ground state and the excited state at site i (i=1,2) as $|i\rangle$ and $|i^*\rangle$ respectively, we want the transition rate from the initial state $|1^*2\rangle$ to the final state $|12^*\rangle$. In the radiationless case the Hamiltonian contains a term which couples the initial and the final states directly. The matrix element is designated as

$$J = \langle 12^*|H|1^*2\rangle \qquad (1\text{-}9)$$

The coupling J is due to Coulamb interaction between the electrons at site 1 and 2 and is of the form of multipolar or exchange interactions. We consider here a rather high concentration of activators so that the mean distance between activator sites is short, the electrostatic coupling is strong, and the overlap of the wave functions is large. In this case the energy transfer occurs radiationlessly.

For the one phonon assisted energy transfer we consider the transition from the initial state

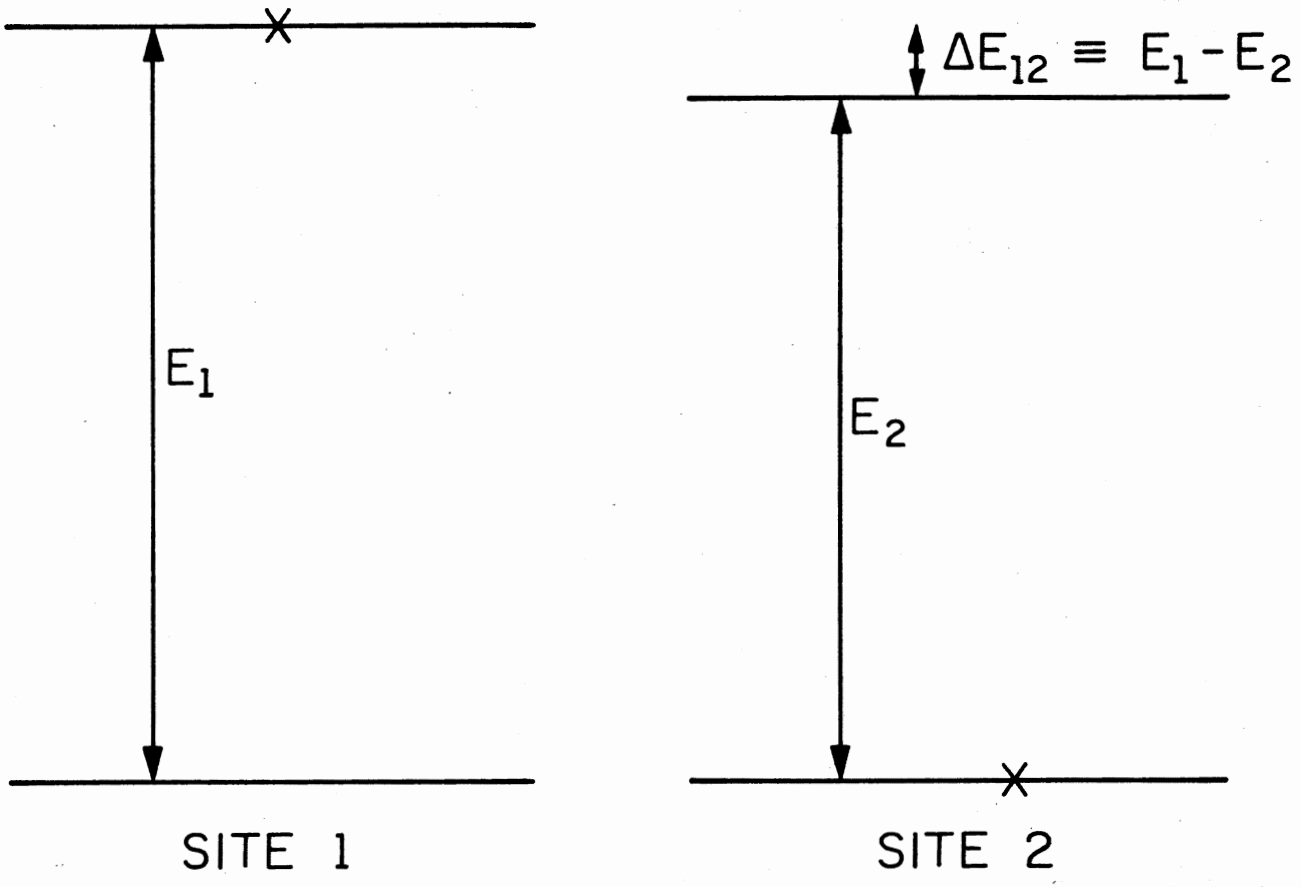

Figure 1. Schematic Diagram Indicating Ground and Excited States of Two Sites and Various Mechanisms of One and Two Phonon Processes Among These Two Sites

$$|i\rangle = |1^*2, n_{sq}\rangle \tag{1-10}$$

of Figure 1 to the final state

$$|f\rangle = |12^*, n_{sq} \pm 1\rangle \quad . \tag{1-11}$$

The lattice vibration states are represented by the Bose factor n_{sq} for the wave vector $\vec{q}$ and polarization s. The plus and minus sign represent the emission and absorption processes respectively.

According to time dependent perturbation theory, the two site jump rate is:

$$W_{2 \leftarrow 1} = \frac{2\pi}{\hbar} \sum_{s,q} |t_{f \leftarrow i}|^2 \delta(\hbar\omega_{sq} \pm \Delta E_{12}) \tag{1-12}$$

where $\omega_{s,q}$ is the phonon frequency and δ is the Dirac delta function. The transition matrix element $t_{f \leftarrow i}$ is then given by

$$t_{f \leftarrow i} = \langle f|H|i\rangle + \sum_{m_1} \frac{\langle f|H|m_1\rangle\langle m_1|H|i\rangle}{\varepsilon_i - \varepsilon_{m_1}} + \sum_{m_1 m_2} \frac{\langle f|H|m_2\rangle\langle m_2|H|m_1\rangle\langle m_1|H|i\rangle}{(\varepsilon_i - \varepsilon_{m_i})(\varepsilon_i - \varepsilon_{m_2})} + \ldots \tag{1-13}$$

where ε_m represents the system energy of the intermediate states "m."

For the one phonon process only the second term in Eq. (1-13) connects the states $|f\rangle$ and $|i\rangle$. There are two possibilities for the intermediate states:

$$|m_i'\rangle = |1^*2, n_{sq} \pm 1\rangle$$

and (1-14)

$$|m_1''\rangle = |12^*, n_{sq}\rangle \quad .$$

Then the energies in the denominators of the second term are

$$\varepsilon_i = \varepsilon_f = E_i$$

$$\varepsilon_{m_1}' = E_1 \pm \hbar\omega_{sq} \qquad (1\text{-}15)$$

$$\varepsilon_{m_1}'' = E_2 \quad .$$

Substituting Eqs. (1-14) and (1-15) in Eq. (1-13) and keeping only the second term, one has:

$$t_{f \leftarrow i} = \sum_{j=1,2} \frac{\langle 12^*, n_{sq} \pm 1|H|1^*2, n_{sq} \pm 1\rangle\langle 1^*2, n_{sq} \pm 1|H(j)|1^*2, n_{sq}\rangle}{E_1 - (E_1 \pm \hbar\omega_{sq})} \qquad (1\text{-}16)$$

$$+ \sum_{j=1,2} \frac{\langle 12^*, n_{sq} \pm 1|H(j)|12^*, n_{sq}\rangle\langle 12^*, n_{sq}|H|1^*2, n_{sq}\rangle}{(E_1 - E_2)} \quad .$$

The H(j) indicates that the phonon emission or absorption occurs at the sites j=1,2.

From Eq. (1-9) one has

$$\langle 12^*, n_{sq} \pm 1|H|1^*2, n_{sq} \pm 1\rangle = \langle 12^*, n_{sq}|H|1^*2, n_{sq}\rangle = J \quad . \qquad (1\text{-}17)$$

We define

$$\langle 1^*2, n_{sq\mp 1}|H(1)|1^*2, n_{sq}\rangle \equiv f(1)\langle n_{sq\mp 1}|\varepsilon(1)|n_{sq}\rangle$$

$$\langle 1^*2, n_{sq\mp 1}|H(2)|1^*2, n_{sq}\rangle \equiv g(2)\langle n_{sq\mp 1}|\varepsilon(2)|n_{sq}\rangle \qquad (1\text{-}18)$$

Here $\varepsilon(j)$ $(j=1,2)$ represents the strain at site j and f(j) and g(j) stand for the spin-phonon coupling strength for the first excited level and the ground level at the site j respectively. Then inserting Eqs. (1-17) and (1-18) in Eq. (1-16) and making use of

$$\mp\hbar\omega_q = \mp \Delta E_{12}$$

and

$$\langle n_{sq\mp 1}|\varepsilon(j)|n_{sq}\rangle = \langle n_{sq\mp 1}|\varepsilon|n_{sq}\rangle \exp[\bar{+}iq\cdot r_j] \qquad (1\text{-}19)$$

where r_j is the position vector of the jt_h site and ε is the strain at r=0, one finds for the transition matrix element:

$$t_{f\leftarrow i} = \frac{J\langle n_{sq\mp 1}|\varepsilon|n_{sq}\rangle \exp[\bar{+}iq\cdot r_2]}{-\Delta E_{12}} \quad x$$

$$[(f(1)-g(1))e^{\mp iq\cdot r} - (f(2)-g(2))] \qquad (1\text{-}20)$$

here we wrote $r=r_2-r_1$.

The fact that only the differences of the spin-phonon coupling constants in the excited and in the ground state are involved in Eq. (1-20), is very convenient because these quantities can be obtained from static stress measurements. Now if one makes the assumption that the spin-phonon coupling constants are site-independent in other words

$$f(j) \equiv f \qquad \text{and} \qquad g(j) \equiv g$$

then the energy transfer rate W of Eq. (1-12) becomes:

$$W_{2 \leftarrow 1} = \frac{2\pi J^2 (f-g)^2}{\hbar (\Delta E_{12})^2} \sum_{sq} |\langle n_{sq} \mp 1 | \varepsilon | n_{sq} \rangle|^2 h^I(q,r)\ \delta(\omega_{sq} \mp \Delta E_{12}) \tag{1-21}$$

The factor $h^I(q,r)$ is called the coherence factor and is given by:

$$h^I(q,r) = |e^{iq\cdot r} - 1|^2 . \tag{1-22}$$

One can distinguish two cases: the case of large energy mismatch and the case of small energy mismatch.

In order to evaluate the energy transfer rate of Eq. (1-21) we will make use of the Debye approximation:

$$\sum_{sq} F(q) = \frac{V}{2\pi^2} \sum_s \frac{1}{v_s^3} \int_0^{\omega_{SD}} \langle F(q) \rangle_\Omega \omega^2 d\omega \tag{1-23}$$

where $\omega = q v_s$ and V, v_s, ω_{SD} are the volume of the sample, the sound velocity and the Debye frequency respectively, and $\langle . \ . \ . \rangle_\Omega$ denotes the angular average.

Large Energy Mismatch

In cases like rare-earth paramagnetic impurities in glasses the energy disorder is large (of the order of $100 cm^{-1}$) and the wavelength of the phonons (i.e. $k\omega_{sq} = |\Delta F_{12}|$) is shorter than the separation of the two sites that we consider

$$qr>1 \qquad (\hbar\omega_{sq} = |\Delta E_{12}|) \ . \tag{1-24}$$

Then when we make directional averaging of the coherence factors, the interference term vanishes leaving the coherence factor

$$\langle h^I(q,r)\rangle_\omega = 2 \ .$$

The i j component of the strain is given by

$$\varepsilon_{ij} = \sum_{sq} 1/2 \left(\frac{\hbar}{2MN\omega_{sq}}\right)^{1/2} (a^+_{sq}+a^-_{sq})(e_{s,i}q_j+e_{s,j}q_i) \tag{1-25}$$

where M,N are mass of the ion, total number of lattice sites, a^+_{sq}, a^-_{sq} are creation and destruction operators of a phonon mode (s,q) and e_s is the polarization vector.

The energy transfer rate is then obtained from Eqs. (1-21) and (1-23):

$$W_{2\leftarrow 1} = \frac{J^2(f-g)^2|\Delta E_{12}|}{\pi\hbar^4\rho}\left(\sum_s \frac{\alpha_s}{v_s^5}\right)\begin{bmatrix} n(|\Delta E_{12}|)+1 \\ n(|\Delta E_{12}|) \end{bmatrix} \text{ for } \begin{bmatrix} \text{emission} \\ \text{absorption} \end{bmatrix}. \tag{1-26}$$

Here $n(x)(\equiv\frac{1}{e^{\beta x}-1})$ is the Bose factor, $\rho(\equiv\frac{KM}{V})$ is the density and α_s is defined by

$$1/4\langle(e_{si}q_j+e_{sj}q_i)^2\rangle_\Omega \equiv \alpha_s q^2 \ . \tag{1-27}$$

In the high temperature limit Eq. (1-26) reduces to

$$W_{2 \leftarrow 1} = \frac{J^2(f-g)^2}{\pi\hbar^4\rho} \left(\sum_s \frac{\alpha_s}{\nu_s^5} \right) k_B T \tag{1-28}$$

This is independent of the energy mismatch and linear in temperature.

Small Energy Mismatch

In this case when the energy mismatch is very small the wavelength of the phonons becomes much larger than the separation between the two sites. In other words

$$qr \ll 1 \quad (\hbar\omega_q = |\Delta E_{12}|) \tag{1-29}$$

the coherence factor becomes very small which combined with the small density of phonon states, makes the transfer rate very small. The angular average of the coherence factor becomes

$$\langle h^I(q,r) \rangle_\Omega \simeq \frac{(qr)^2}{3}$$

and using the Debye approximation the transfer rate is given by

$$W_{2 \leftarrow 1} = \frac{J^2(f-g)^2 |\Delta E_{12}|^3 r^2}{6\pi\hbar^6\rho} \left(\sum_s \frac{\alpha_s}{\nu_s^7} \right) \begin{cases} n(|\Delta E_{12}|)+1 \\ n(|\Delta E_{12}|) \end{cases} \text{for} \begin{cases} \text{emission} \\ \text{absorption} \end{cases} \tag{1-30}$$

in the high temperature limit Eq. (1-30) reduces to

$$W_{2 \leftarrow 1} = \frac{J^2(f-g)^2 |\Delta E_{12}|^2 r^2}{6\pi\hbar^6\rho} \left(\sum_s \frac{\alpha_s}{\nu_s^7} \right) k_\beta T \quad . \tag{1-31}$$

This is smaller than the rate for a large energy mismatch if we compare it with Eq. (1-28) by a factor

$$\frac{1}{6}\left(\frac{\Delta E_{12}r}{v_s}\right)^2 \tag{1-32}$$

that is the average coherence factor.

In summary the one-phonon assisted energy transfer rate is small for small energy mismatch due to a small phonon density of states and mostly due to the small coherence factor. At sufficiently high temperatures though, a faster rate is obtained due to two-phonon assisted processes. Here two phonons with large energies $\hbar\omega_{s'q'}$ and $\hbar\omega_{sq}$ are emitted and absorbed respectively, conserving the total energy $\hbar\omega_{s'q'} - \hbar\omega_{sq} = \Delta E_{12}$. In cases of small energy mismatch the one-phonon processes are the dominant, inspite of the higher order of the two-phonon processes. This is due to the fact that a large number of phonon modes are available for phonons of large energy and the coherence factor does not become small due to the large wave vectors of the phonons involved.

In the case of two phonon assisted energy transfer the energies of the phonons that are involved in these processes are either $k_\beta T$ or equal to a certain resonant energy that we will examine later. In the second the energy is conserved for the intermediate state involving the resonant level. These processes are called "nonresonant" and "resonant" processes respectively.

Considering the two-phonon, three-stage processes, one finds that the second and third terms of the transition matrix in Eq. (1-13) are of importance. The t-matrix then contains a number of terms corresponding to possible intermediate states in the perturbation series that connect the initial state ($|i\rangle$) and the final state ($|f\rangle$), i.e.:

$$|i\rangle = |1^*2, n_{sq}, n_{s'q'}\rangle$$
$$|f\rangle = |12^*, n_{sq}-1, n_{s'q'}+1\rangle \qquad (1\text{-}33a)$$

The energies of these states are

$$\varepsilon_i = E_1 \quad ,$$
$$\varepsilon_f = E_2 - \hbar\omega_{sq} + \hbar\omega_{s'q'} \qquad (1\text{-}33b)$$

respectively and the transition rate will be:

$$W_{2 \leftarrow 1} = \frac{2\pi}{\hbar} \sum_{ss'qq'} |t_{f \leftarrow i}|^2 \, \delta \, (\hbar\omega_{s'q'} - \hbar\omega_{sq} - \Delta E_{12}) \qquad (1\text{-}34)$$

It is evident that the number of terms in the t-matrix make the evaluation of the transition rate almost impossible. One way of attacking the problem is to separate the terms in groups that each one is dominant at different temperature regions, depending on various parameters. One can distinguish, then, four different schemes.

Nonresonant-Phonon-Assisted Energy Transfer Within the First Excited Level: One Phonon

In this case the one-phonon-spin Hamiltonian diagonal in the electronic state is used to the second order. The t-matrix here

consists of three stage processes and the important term is the fourth term of Eq. (1-13).

Figure 2 shows pictorially a typical perturbation chain. In the beginning a phonon (wave-like line) of mode q is absorbed at site 1 resulting in a first intermediate state ($|m_1>$). The electronic state remains the same. Then, electrostatic or exchange interaction takes place between site 1 and site 2 and the result is the second intermediate state ($|m_2>$). Where the site 1 is in the ground state and the site 2 is in the first excited state. Finally, a phonon of mode q´ is emitted at site 2. The intermediate states and their energies are:

$$|m_1> = |1^*2, n_{sq}-1, n_{sq'}>$$
$$|m_2> = |12^*, n_{sq}-1, n_{sq'}> \qquad (1\text{-}35a)$$

and

$$\varepsilon_{m_1} = E_1 - \hbar\omega_{sq}$$
$$\varepsilon_{m_2} = E_2 - \hbar\omega_{sq} \qquad (1\text{-}35b)$$

From Eqs. (1-17), (1-18), (1-19), (1-33), and (1-35) the third term of (1-13) gives for the t-matrix and for the scheme of Figure 2

$$\frac{Jf(1)f(2)}{\hbar\omega_{sq}\hbar\omega_{s'q'}} <n_{sq}-1|\varepsilon|n_{sq}><n_{s'q'}+1|\varepsilon|n_{s'q'}>\exp\,[iq\cdot r_1 - iq\cdot r_2] \qquad (1\text{-}36)$$

But by ordering the different processes of Figure 2 in different sequence one obtains six different combinations. So the contribution of all these six cases has to be taken into account. Then the t-matrix becomes

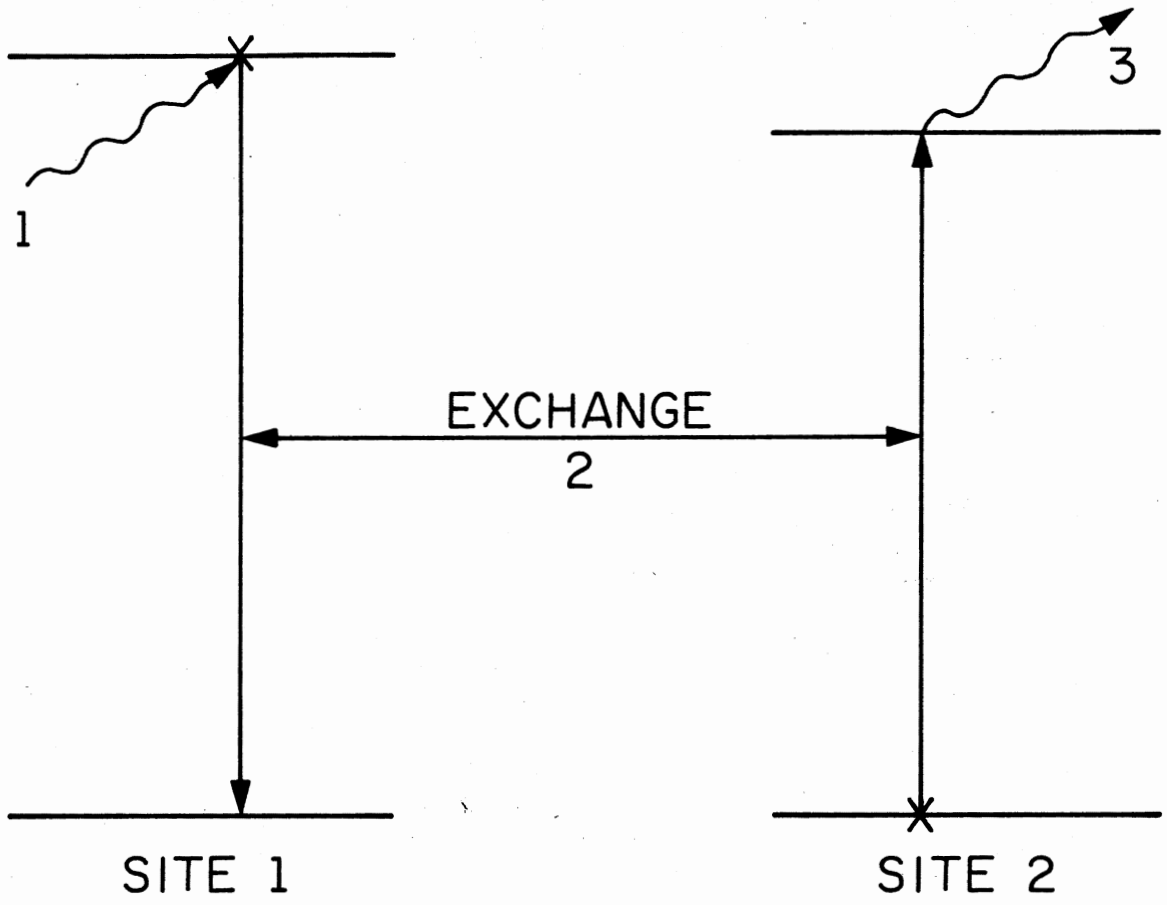

Figure 2. Schematic Diagram Indicating Ground and Excited States of Two Sites and Various Mechanisms of One and Two Phonon Processes Among These Two Sites

$$\frac{J}{\hbar\omega_{sq}\hbar\omega_{s'q'}} \langle n_{sq}-1|\varepsilon|n_{sq}\rangle\langle n_{s'q'}+1|\varepsilon|n_{s'q'}\rangle\Big\{f(1)f(2)(\exp[iq\cdot r_1-iq'\cdot r_2]+\exp$$

$$[-iq'\cdot r_1+iq\cdot r_2]) - f(1)^2 \exp[i(q-q')\cdot r_1] - f(2)^2 \exp[i(q-q')\cdot r_2]\Big\} \tag{1-37}$$

Here the relationship $\hbar\omega_{s'q'}-\hbar\omega_{sq} = \Delta E_{12}$ Has been taken into account.

For the case of spin phonon interaction in the ground state there are six schemes like Figure 2 leading to an equation the same as (1-37) except the parameters f are replaced by g. For the case that there are spin-phonon interactions involved in both the ground and the first excited state, there are twelve more schemes and the result is like before to replace f by f-g in Eq. (1-37). Here the assumption that f(j) and g(j) are site independent has been made. Then the transfer rate is given by:

$$W_{2\leftarrow 1}^{\text{nonres. I}} = \frac{2\pi}{\hbar} \sum_{ss'qq'} [J^2(f-g)^4/\hbar^2(\omega_{sq}\omega_{s'q'})^2]|\langle n_{s'q'}+1|\varepsilon|n_{s'q'}\rangle \tag{1-38}$$

$$\langle n_{sq}-1|\varepsilon|n_{sq}\rangle|^2 \, h^{II}(q, q'; r)\, \delta(\hbar\omega_{s'q'}-\hbar\omega_{sq}-\Delta E_{12})$$

where

$$h^{II}(q,q';r) = |e^{-iq'\cdot r} + e^{iq\cdot r} - 1 - e^{i(q-q')\cdot r}|^2 \tag{1-39}$$

In the high temperature limit ($|i\varepsilon\beta/\Delta E_{12}|<<1$) and assuming that the main contribution arises from the high energy phonons ($i\varepsilon qr\gtrsim 1$) the transfer rate becomes:

$$W_{2\leftarrow 1}^{\text{nonres. I}} = \frac{J^2(f-g)^4}{2\pi^3\hbar^7\rho^2}\left(\sum_s \frac{\alpha_s}{\nu_s^5}\right)^2 (k_\beta T)^3 \, I_2 \quad . \tag{1-40}$$

Here the Debye approximation was used.

$$I_n = \int_0^{\theta_D/T} \frac{x^n dx}{(e^x-1)(1-e^{-x})} \quad ; \quad x = \frac{\hbar\omega_{sq}}{k_\beta T} \tag{1-41}$$

where θ_D is the Debye temperature.

When the upper limit of the integral in (1-41) becomes $\theta_{D/T} >> 1$ then $I_n \to n!$. So that for n=2, $x \simeq 2$ so $\hbar\omega_{sq} = 2k_\beta T$. And (1-40) is valid if $qr>1$, for $\hbar\omega_{sq} = 2k_\beta T$. The rate in (1-40) is proportional to T^{-3} in the limit $T << \theta_D$. And summarizing, the rate is proportional to T^{-3} in the region $|\Delta E_{12}| << k_\beta T << k_\beta \theta_D$ if the temperature is sufficiently high so that $qr>1$ for the phonons of energy $2k_\beta T$.

Nonresonant-Phonon-Assisted Energy Transfer Within the First Excited Level: Two Phonons

In this mechanism the two-phonon-spin coupling is used to the first order. The t-matrix consists of two stage-processes. And the second term of Eq. (1-13) is dominant. Figure 3 shows a typical perturbation chain. Here a simultaneous one phonon absorption and emission occur in the first excited state of site 1 and then exchange interaction takes place. There is one intermediate state ($|m\rangle$) and it is given by

$$|m\rangle = |1^*2, n_{sq}-1, n_{s'q'}+1\rangle$$

with energy

$$\varepsilon_m = E_1 - \hbar\omega_{sq} + \hbar\omega_{s'q'} \tag{1-42}$$

From (1-42) and the second term of (1-13) one has

$$\frac{Jf_2(1)}{-\Delta E_{12}} \langle n_{sq}-1, n_{s'q'}+1 | \varepsilon^2 | n_{sq}, n_{s'q'} \exp\,[i(q-q')\cdot r_1] \tag{1-43}$$

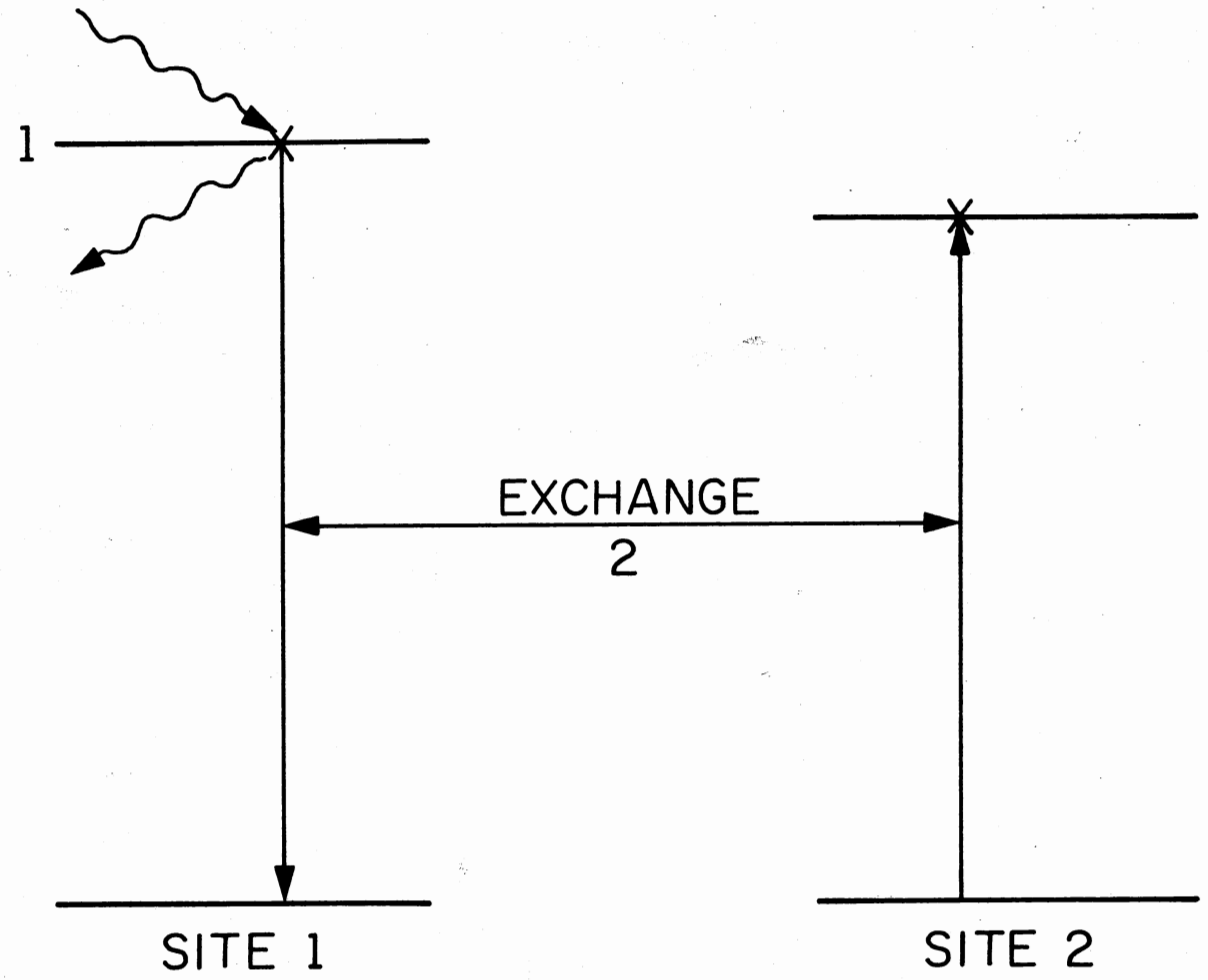

Figure 3. Schematic Diagram Indicating Ground and Excited States of Two Sites and Various Mechanisms of One and Two Phonon Processes Among These Two sites

where $f_2(j)$ is the strength of the quadratic spin-phonon matrix element in the first excited state at the site j. There are two more schemes of this type and one additional for the quadratic spin-phonon interaction in the ground state with a strength $g_2(j)$. So the total transition matrix becomes

$$t_{f \leftarrow i} = \frac{J\langle n_{sq}-1, n_{s'q'}+1|\varepsilon^2|n_{sq}, n_{s'q'}\rangle}{\Delta E_{12}} \Big\{ (f_2(2)-g_2(2)) \exp[i(q-q')\cdot r_2] - (f_2(1)-g_2(1)) \exp[i(q-q')\cdot r_1] \Big\} \tag{1-44}$$

Under the assumption that f and g are site independent, the transition rate will be:

$$W_{2\leftarrow 1}^{\text{nonres. II}} = \frac{2\pi}{\hbar} \sum_{ss'qq'} (J/\Delta E_{12})^2 (f_2-g_2)^2 |\langle n_{sq}-1, n_{s'q'}+1|\varepsilon^2|n_{sq}, n_{s'q'}|^2 h^I(q-q', r)\, \delta(\hbar\omega_{s'q'} - \hbar\omega_{sq} - \Delta E_{12}) \tag{1-45}$$

In the high temperature limit ($\beta|\Delta E_{12}|<<1$) under the assumption that the dominant phonons are the ones with short wavelength ($qr>1$) the average coherence factor is

$$\langle h^I \rangle_{av} \sim 2$$

and

$$W_{2\leftarrow 1}^{\text{nonres. II}} = \frac{J^2(f_2-g_2)^2}{4\pi^3\hbar^7\rho^2(\Delta E_{12})^2} \left(\sum_s \frac{\alpha_s}{\nu_s^5} \right) I_6 (k_\beta T)^7 \tag{1-46}$$

It should be noted that the rate here is inversely proportional to the square of the energy mismatch. The dominant contribution to I_6 arises from phonons of energy $\hbar\omega_{sq} \sim 6k_\beta T$. In conclusion Eq. (1-46) is obtained in the region $|\Delta E_{12}| << k_\beta T << k_\beta \theta_D$ and the rate is proportional to T^{-7} in high temperature region where $qr>1$ for $\hbar\omega_q \sim 6k_\beta T$. In the limit $\theta_{D/T} >> 1$ the ratio of the two rates Eq. (1-40) and Eq. (1-46) is:

$$\frac{W_{2\leftarrow 1}^{\text{nonres. I}}}{W_{2\leftarrow 1}^{\text{nonres. II}}} = \frac{(f-g)^4(\Delta E_{12})^2}{180(f_2-g_2)^2(k_\beta T)^4} \tag{1-47}$$

Resonant Phonon-Assisted Energy Transfer
Via the Second Excited Level

There are systems that have a second excited state within the reach of a phonon energy from the first excited state. This state will be symbolized by ($|j^{**}\rangle$). Energy conservation can be obtained in this case by a three stage process as illustrated in Figure 4a. In the beginning a phonon of energy $\hbar\omega_{sq}$ is absorbed and the electronic state at site 1 changes into the upper level $|1^{**}\rangle$. Then, a phonon of energy $\hbar\omega_{s'q'}$ is emitted and the electronic state at site 1 returns to the first excited level. Last, the exchange interaction occurs between sites 1 and 2. The intermediate states $|m_1\rangle$ and $|m_2\rangle$ and their energies will be

$$\left.\begin{aligned} |m_1\rangle &= |1^{**}2, n_{sq}-1, n_{s'q'}\rangle \\ |m_2\rangle &= |1^{*}2, n_{sq}-1, n_{s'q'}+1\rangle \\ \varepsilon_{m_1} &= E_1 + \delta - \hbar\omega_{sq} \\ \varepsilon_{m_2} &= E_1 - \hbar\omega_{sq} + \hbar\omega_{s'q'} \end{aligned}\right] \tag{1-48}$$

δ here represents the energy separation between the two excited levels. If we write

$$\langle 1^{**}|H|1^{*}\rangle = A\,\varepsilon\,(1) \tag{1-49}$$

the t-matrix for the process of Figure 4a is:

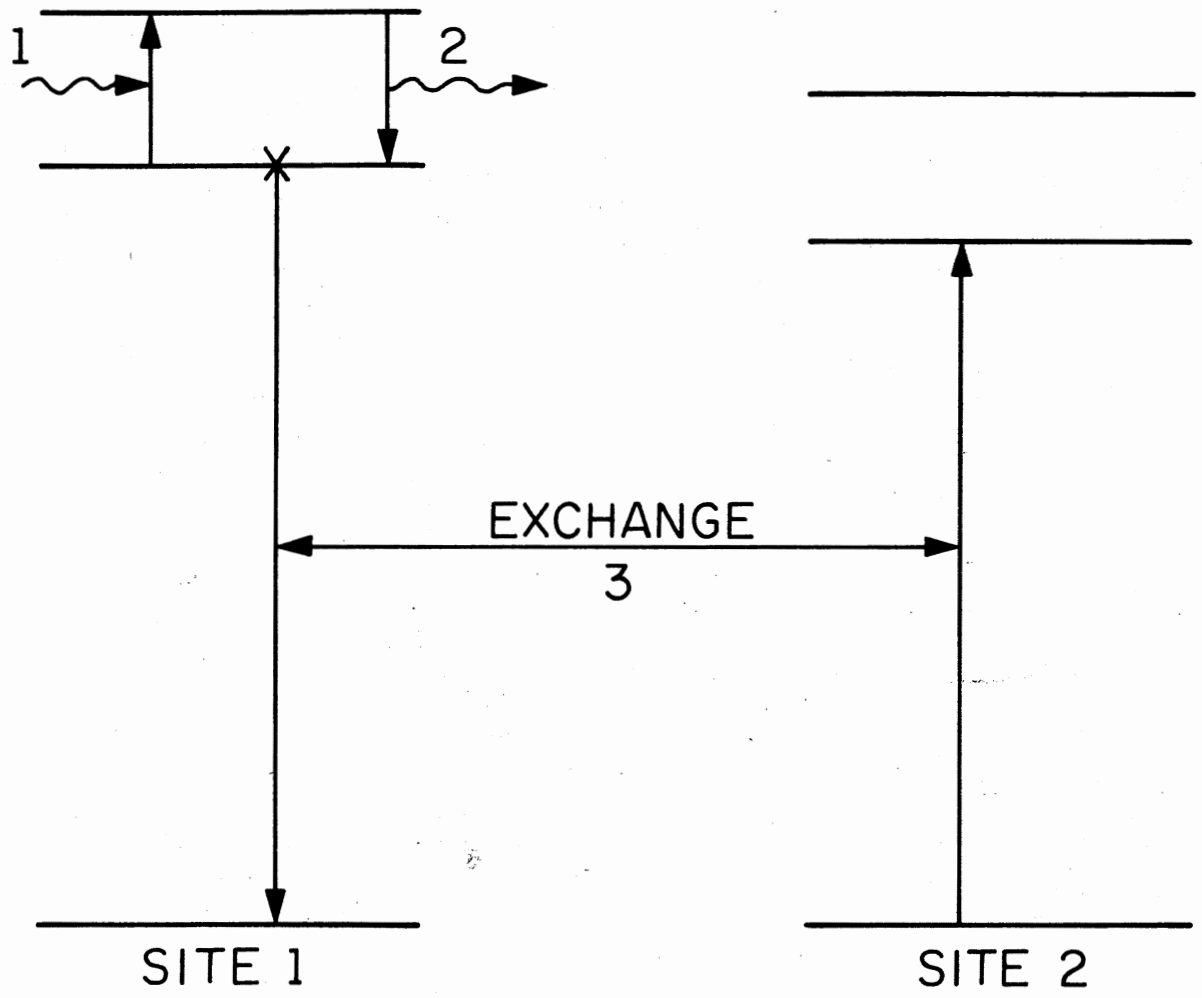

Figure 4a. Schematic Diagram Indicating Ground and Excited States of Two Sites and Various Mechanisms of One and Two Phonon Processes Among These Two Sites

$$t^{(a)}_{f \leftarrow 1} = \frac{J}{\Delta E_{12}} \frac{|A|^2}{\delta - \hbar\omega_{sq} + i\Gamma_2} \langle n_{sq}-1, n_{s'q'}+1 | \varepsilon^2(1) | n_{sq}, n_{s'q'} \rangle \qquad (1\text{-}50)$$

Here the imaginary quantity $i\Gamma_2$ has been added to the denominator to avoid divergence at $\hbar\omega_{sq}=\delta$. Γ_2 is the phonon induced half width of the upper excited level and is given by

$$\Gamma_2 = \pi \sum_{sq} |A\langle n_{sq}+1 | \varepsilon | n_{sq} \rangle|^2 \, (\delta - \hbar\omega_{sq}) \qquad (1\text{-}51)$$

There are two more schemes like Figure 4a namely the ones illustrated in Figure 4b and 4c. Their contributions to the t-matrix are:

$$t^{(b)}_{f \leftarrow i} = - \frac{J|A|^2}{\Delta E_{12}} \frac{\langle n_{sq}-1, n_{s'q'}+1 | \varepsilon^2(2) | n_{sq}, n_{s'q'} \rangle}{\delta - \hbar\omega_{s'q'} + i\Gamma_2} \qquad (1\text{-}52)$$

and

$$t^{(c)}_{f \leftarrow 1} = \frac{J_2 |A^2| \langle n_{sq}-1 | \varepsilon(1) | n_{sq} \rangle \langle n_{s'q'}+1 | \varepsilon(2) | n_{s'q'} \rangle}{(\delta - \hbar\omega_{sq} + i\Gamma_2)(\delta - \hbar\omega_{s'q'} + i\Gamma_2)} \qquad (1\text{-}53)$$

where J_2 is the exchange or generally electrostatic interaction involving the second excited levels at site 1 and 2, and only the resonant phonons ($\hbar\omega_{sq} \simeq \delta$, $\hbar\omega_{s'q'} \simeq \delta$) give rise to the contribution to the transition rate.

Eq. (1-50), (1-52), (1-53) and using (1-19) result in the following expression for the t-matrix.

$$t'_{f \leftarrow i} = |A|^2 \langle n_{sq}-1, n_{s'q'}+1 | \varepsilon^2 | n_{sq}, n_{s'q'} \rangle \exp[i(q-q')\cdot r_1] \left\{ \frac{J}{\Delta E_{12}(\delta - \hbar\omega_{sq} + i\Gamma_2)} \right.$$

$$\left. - \frac{J \exp[i(q-q')\cdot r]}{\Delta E_{12}(\delta - \hbar\omega_{s'q'} + i\Gamma_2)} + \frac{J_2 \exp[-iq'\cdot r]}{(\delta - \hbar\omega_{sq} + i\Gamma_2)(\delta - \hbar\omega_{s'q'} + i\Gamma_2)} \right. \qquad (1\text{-}54)$$

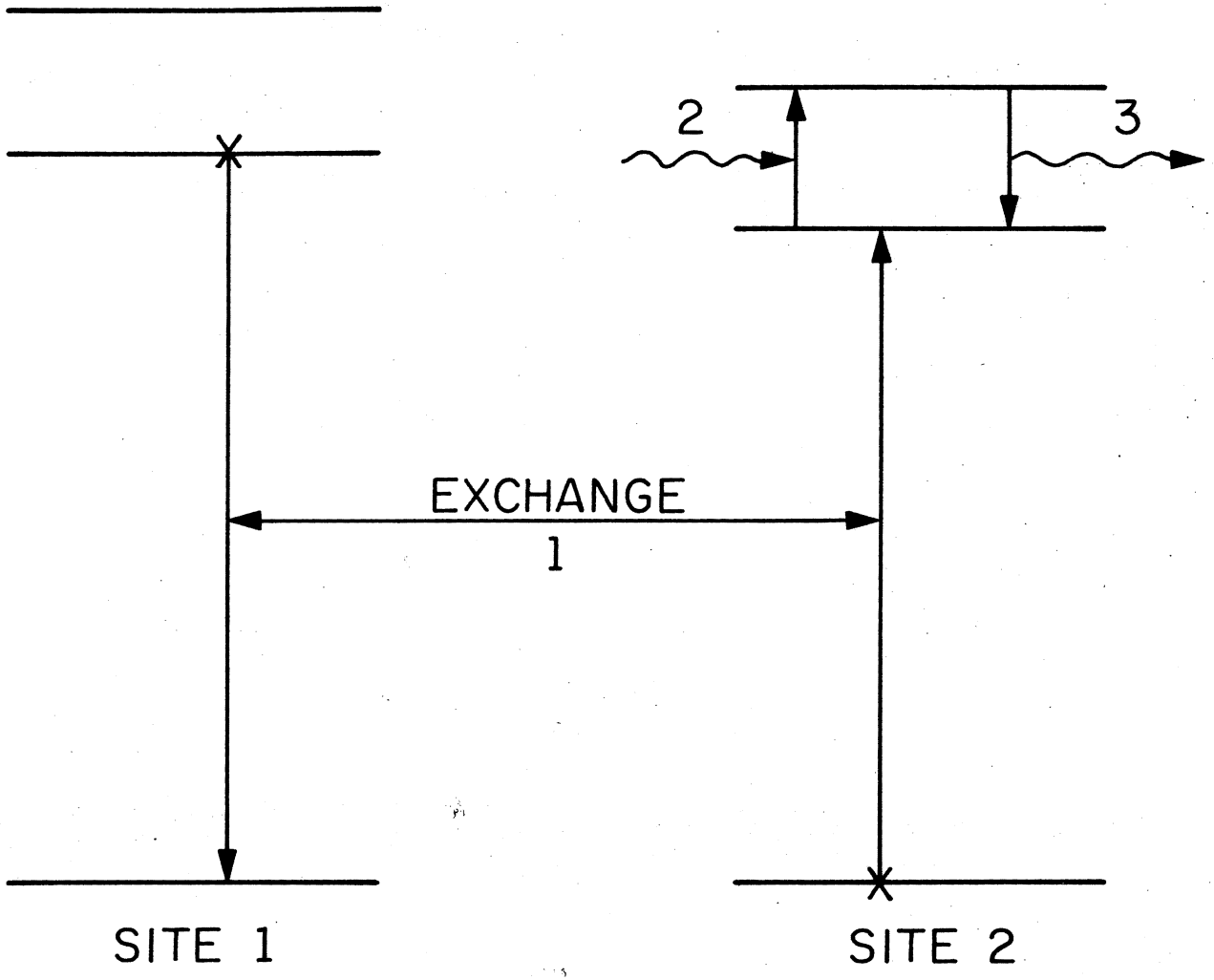

Figure 4b. Schematic Diagram Indicating Ground and Excited States of Two Sites and Various Mechanisms of One and Two Phonon Processes Among These Two Sites

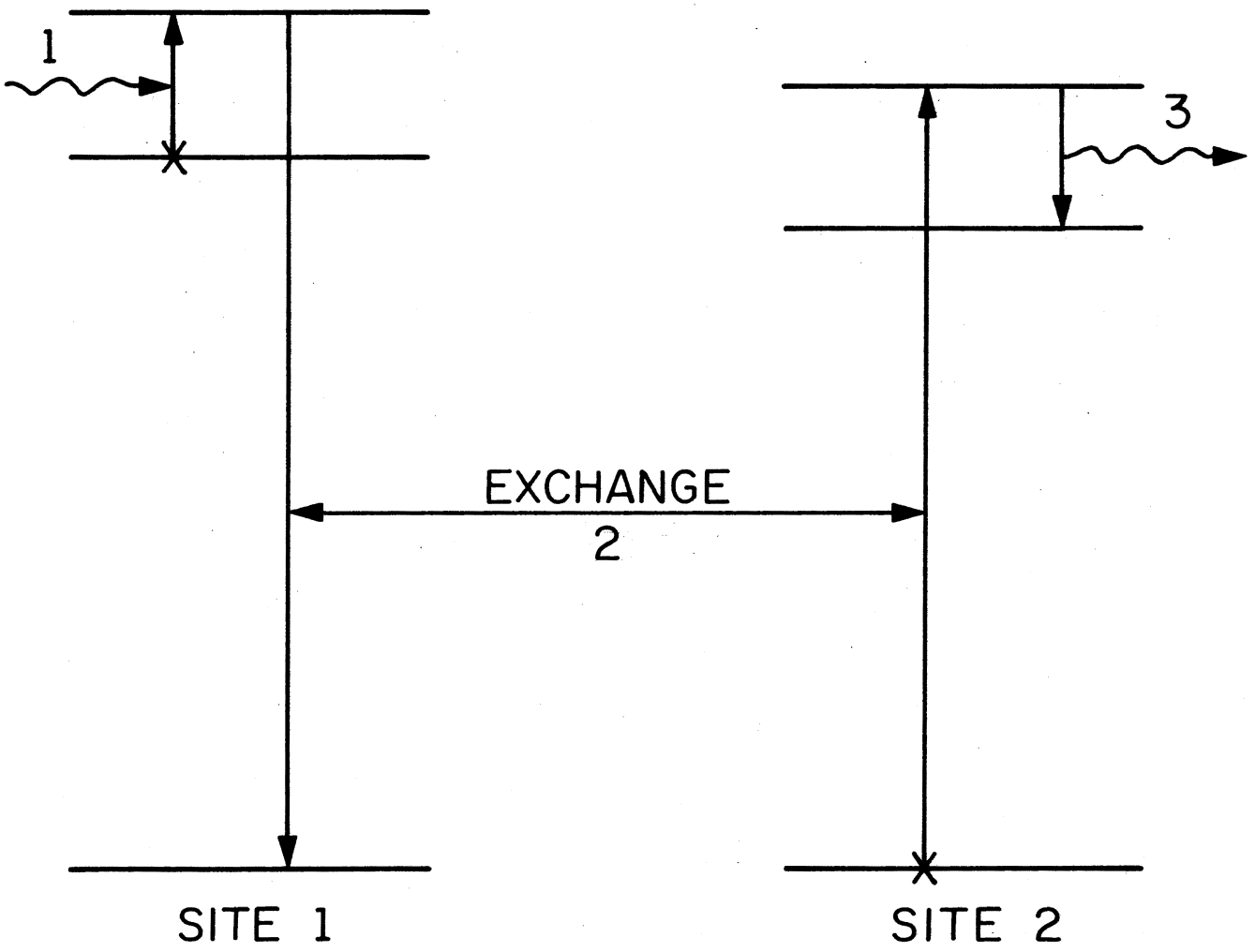

Figure 4c. Schematic Diagram Indicating Ground and Excited States of Two Sites and Various Mechanisms of One and Two Phonon Processes Among These Two Sites

The t-matrix of Eq. (1-54) substituted into Eq. (1-34) gives the transition rate. In order to simplify the calculation the energy separation δ is assumed to be sufficiently large so that the wave length of the resonant phonons is shorter than the distance between the two sites

$$qr>1 \qquad (\hbar\omega_q = \delta) \tag{1-55}$$

and that

$$|\Delta E_{12}| << \delta \ . \tag{1-56}$$

Then the transition rate becomes

$$W_{2\leftarrow 1}^{res} = \frac{2\pi}{\hbar} \sum_{ss'qq'} |A^2 <n_{sq}-1, n_{s'q'}+1|\varepsilon^2|n_{sq}, n_{s'q'}>|^2 \left\{ \frac{J^2}{(\Delta E_{12})^2} \left(\frac{1}{(\delta-\hbar\omega_{sq})^2+\Gamma_2^2} + \frac{1}{(\delta-\hbar\omega_{s'q'})^2+\Gamma_2^2} \right) + \frac{J_2^2}{[(\delta-\hbar\omega_{sq})^2+\Gamma_2^2][(\delta-\hbar\omega_{s'q'})^2+\Gamma_2^2]} \right\} \tag{1-57}$$

Since typically $\Gamma_2 < 1 cm^{-1}$ it is logical to assume that the Bose factors do not vary significantly over the range $\hbar\omega_{sq} \sim \Gamma_2$, i.e.

$$\Gamma_2 << k_\beta T \tag{1-58}$$

Then the third term of Eq. (1-57), which we symbolize as III, is of the form:

$$III = \int_{-\infty}^{\infty} dx \ \frac{f(x)}{[(\delta-x)^2+\Gamma_2^2][(\delta-\Delta E_{12}-x)^2+\Gamma_2^2]}$$

where $f(x)$ has little variation over the range $dx \sim \Gamma_2$ near the resonances. Then

$$III \simeq [f(\delta) + f(\delta-\Delta E_{12})] \int_{-\infty}^{\infty} \frac{dx}{[(\delta-x)^2+\Gamma_2^2][(\delta-\Delta E_{12}-x)^2+\Gamma_2^2]}$$

$$= [f(\delta) + f(\delta-\Delta E_{12})] \frac{2\pi}{\Gamma_2} \frac{1}{(\Delta E_{12})^2+(2\Gamma_2)^2}$$

for

$$|\Delta E_{12}| >> \Gamma_2$$

and

$$III \simeq f(\delta)\ \frac{\pi}{2\Gamma_2^3}$$

for

$$|\Delta E_{12}| << \Gamma_2$$

Using the above on the third term of Eq. (1-57) we obtain the approximation

$$\frac{1}{[(\delta-\hbar\omega_{sq})^2+\Gamma_2^2][(\delta-\hbar\omega_{s'q'})^2+\Gamma_2^2]} \simeq \frac{2}{(\Delta E_{12})^2+(2\sqrt{2}\ \Gamma_2)^2} \tag{1-59}$$

$$\times\left\{\frac{1}{(\delta-\omega_{sq})^2+\Gamma_2^2}+\frac{1}{(\delta-\hbar\omega_{s'q'})^2+\Gamma_2^2}\right\}$$

where

$$\frac{1}{\pi}\ \frac{\Gamma_2}{(\delta-\hbar\omega_{sq})^2+\Gamma_2} \simeq \delta\ (\delta-\hbar\omega_{sq}) \tag{1-60}$$

has been used. Introducing (1-59) and (1-60) in (1-57) we obtain

$$W_{2\leftarrow 1}^{res} = \frac{2\pi^2}{\hbar(\Delta E_{12})^2\Gamma_2}\ \sum_{ss'qq'} |A^2\langle n_{sq}-1, n_{s'q'}+1|\varepsilon^2|n_{sq}, n_{s'q'}\rangle|^2\left\{J^2\right.$$

$$\left.+\frac{2(\Delta E_{12})^2 J_2^2}{(\Delta E_{12})^2+(2\sqrt{2}\Gamma_2)^2}\right\}[\delta(\delta-\hbar\omega_{sq})\delta(\delta+\Delta E_{12}-\hbar\omega_{s'q'})+\delta(\delta-\hbar\omega_{s'q'})\delta(\delta-\Delta E_{12}-$$

$$\hbar\omega_{s'q'})] \tag{1-61}$$

One defines a phonon induced "vertical" transition rate from the first excited to the second excited levels:

$$\omega_{vert.} = \frac{2\pi}{\hbar} \sum_{sq} |A\langle n_{sq}-1|\varepsilon|n_{sq}\rangle|^2 \delta(\delta-\hbar\omega_{sq}) \tag{1-62}$$

Γ_2 is related to $\omega_{vert.}$ through (1-63)

$$\omega_{vert.} = \frac{2}{\hbar} \Gamma_2 e^{-\beta\delta}$$

If we neglect the variation of the phonon density of states between δ and $\delta+\Delta E_{12}$ and make use of (1-51) and (1-62), Eq. (1-61) becomes

$$W_{2\leftarrow 1}^{res} = \left[J^2 + \frac{2(\Delta E_{12})^2 J_2^{\,2}}{(\Delta E_{12})^2+(2\sqrt{2}\Gamma_2)^2} \right] \left[\frac{n(\delta+\Delta E_{12})+1}{n(\delta)+1} + \frac{n(\delta-\Delta E_{12})}{n(\delta)} \right] \frac{\omega_{vert.}}{(\Delta E_{12})^2} \,. \tag{1-64}$$

Assuming

$$k_\beta T \ll \delta \pm \Delta E_{12} \tag{1-65}$$

the transition rate becomes finally

$$W_{2\leftarrow 1}^{res} = \left[J^2 + \frac{2(\Delta E_{12})^2 J_2^{\,2}}{(\Delta E_{12})^2+(2\sqrt{2}\Gamma_2)^2} \right] \frac{1+e^{\beta\Delta E_{12}}}{(\Delta E_{12})^2} \omega_{vert.} \tag{1-66}$$

In the limit

$$\beta|\Delta E_{12}| \ll 1 \tag{1-67}$$

Eq. (1-65) reduces to the result that one obtains using the spectral overlap model.

In summary we obtain the same result with the spectral overlap model if the approximations (1-56), (1-58), (1-65), and (1-67) are valid.

Nonresonant-Phonon-Assisted Energy Transfer

Via the Second Excited Level

Here we consider three-stage virtual processes where the upper excited state is involved. The schemes of Figure 4 are valid but three more processes are added namely the ones in Figure 4 but with the arrows, symbolizing phonon emission and absorption, inverted. The transition matrix for these three new processes following the same order of Figure 4 will be:

$$t''_{f\leftarrow i}=|A|^2\langle n_{sq}-1,n_{s'q'}+1|\varepsilon^2|n_{sq},n_{s'q'}\rangle\left[\frac{Je^{i(q-q')r_1}}{\Delta E_{12}(\delta+\hbar\omega_{s'q'})}-\frac{Je^{i(q-q')\cdot r_2}}{\Delta E_{12}(\delta+\hbar\omega_{sq})}+\frac{J_2e^{i(q\cdot r_2-q'\cdot r_1)}}{(\delta+\hbar\omega_{sq})(\delta+\hbar\omega_{s'q'})}\right] \tag{1-68}$$

If now one combines Eq. (1-54) and Eq. (1-68) one obtains the total transition matrix of the present case namely:

$$t_{f\leftarrow i}=t'_{f\leftarrow i}+t''_{f\leftarrow i}$$

Now if one ignores the effect of the interference between the resonant and nonresonance processes by dropping the imaginary parts from the denominators of Eq. (1-54) then the total t-matrix becomes

$$t_{f\leftarrow i}=t'_{f\leftarrow i}+t''_{f\leftarrow i}=|A|^2\langle n_{sq}-1,n_{s'q'}+1|\varepsilon^2|n_{sq},n_{s'q'}\rangle e^{i(q-q')\cdot r_1}$$

$$\left[\frac{J}{\Delta E_{12}}\left(\frac{1}{\delta-\hbar\omega_{sq}}+\frac{1}{\delta+\hbar\omega_{s'q'}}\right)-\frac{Je^{i(q-q')\cdot r}}{\Delta E_{12}}\left(\frac{1}{\delta-\hbar\omega_{s'q'}}+\frac{1}{\delta+\hbar\omega_{sq}}\right)\right.$$

$$+ J_2 e^{-iq'\cdot r} \left(\frac{1}{(\delta-\hbar\omega_{sq})(\delta-\hbar\omega_{s'q'})} + \frac{e^{i(q+q')\cdot r}}{(\delta+\hbar\omega_{sq})(\delta+\hbar\omega_{s'q'})} \right) \Bigg] \tag{1-69}$$

Now we make use at the assumption (1-56) as well as $J_2 \sim J$. As result the second member of the term proportional to J_2 in Eq. (1-69) is of order $\Delta E_{12}/\delta$ smaller and we drop it. Then Eq. (1-69) can be written as

$$t_{f \leftarrow i} = \frac{|A|^2}{\Delta E_{12}} \langle n_{sq}-1, n_{s'q'}+1 | \varepsilon^2 | n_{sq}, n_{s'q'} \rangle e^{i(q-q')\cdot r_l} \, J \left(\frac{1}{\delta-\hbar\omega_{sq}} + \frac{1}{\delta+\hbar\omega_{s'q'}} \right)$$

$$- J e^{i(q-q')\cdot r} \left(\frac{1}{\delta-\hbar\omega_{s'q'}} + \frac{1}{\delta+\hbar\omega_{sq}} \right) + J_2 e^{-iq'\cdot r}$$

$$\left(\frac{1}{\delta-\hbar\omega_{s'q'}} - \frac{1}{\delta-\hbar\omega_{sq}} \right) \Bigg] \tag{1-70}$$

where $\hbar\omega_{s'q'} - \hbar\omega_{sq} = \Delta E_{12}$ has been used in the last term. We examine the case that

$$|\Delta E_{12}| \ll k_\beta T \ll \delta/6 \tag{1-71}$$

In this case it turns out that the dominant contribution comes from

$$\hbar\omega_{sq} \simeq \hbar\omega_{s'q'} \sim 6k_\beta T \ .$$

In a rough approximation (unless δ is very large) we drop the phonon energies from the denominators of Eq. (1-70), suffering an error of the order of

$$\left(\frac{6k_\beta T}{\delta} \right)^2$$

and we have

$$W_{2\leftarrow 1}^{\text{nonres. III}} = \frac{8\pi J^2}{\delta^2(\Delta E_{12})^2\hbar} \sum_{ss'qq'} |A'^2\langle n_{sq}-1, n_{s'q'}+1|\varepsilon^2|n_{sq}, n_{s'q'}\rangle|^2$$

$$h^I(q-q',r)\delta(\hbar\omega_{s'q'}-\hbar\omega_{sq}-\Delta E_{12}) \tag{1-72}$$

where h^I is the coherence factor given by the Eq. (1-22).

Now considering high temperatures, neglecting ΔE_{12} in the delta function, and using (1-23) and (1-27) as well as the Debye approximation one finds:

$$W_{2\leftarrow 1}^{\text{nonres. III}} = \frac{J^2|A|^4(k_\beta T)^7}{\pi\hbar^7\delta^2(\Delta E_{12})^2\rho^2}\left(\sum_s \frac{\alpha_s}{\nu_s^5}\right)^2 I_6 \tag{1-73}$$

This transition rate can be expressed in terms of Γ_2 (as previously). Here Γ_2 is evaluated as

$$\Gamma_2 = \frac{|A|^2\delta^3}{4\pi\hbar^3\rho}\left(\sum_s \frac{\alpha_s}{\nu_s^5}\right)[n(\delta)+1] \tag{1-74}$$

For $n(\delta)\simeq 0$ combining (1-73) and (1-74) one has finally

$$W_{2\leftarrow 1}^{\text{nonres. III}} = \frac{16T^2(k_\beta T)^7\Gamma_2^2 I_6}{\pi\hbar\delta^8(\Delta E_{12})2}\,. \tag{1-75}$$

To compare the resonant and nonresonant cases one considers the limit $\theta_D >> T$ then $I_6 \simeq 6!$ and taking the ratio of (1-66) and (1-75) one has:

$$\frac{W_{2\leftarrow 1}^{\text{res.}}}{W_{2\leftarrow 1}^{\text{nonres. III}}} = 3.472 \times 10^{-4}\left(\frac{\delta}{\Gamma_2}\right)(\beta\delta)^7 e^{-\beta\delta}\left[1 + \frac{2(\Delta E_{12})^2(J_2/J)^2}{(\Delta E_{12})^2+(2\sqrt{2}\Gamma_2)^2}\right]. \tag{1-76}$$

For

$$T_{max} = \frac{\delta}{7k_\beta} \tag{1-77}$$

the ratio becomes maximum given by:

$$\left(\frac{W^{res}_{2 \leftarrow 1}}{W^{nonres.\ III}_{2 \leftarrow 1}}\right)_{max} = 0.2607 \left(\frac{\delta}{\Gamma_2}\right)\left[1 + \frac{2(\Delta E_{12})^2(J_2/J)^2}{(\Delta E_{12})^2+(2\sqrt{2}\Gamma_2)^2}\right] \quad (1\text{-}78)$$

Because usually $\delta/\Gamma_2 >> 1$ the resonant transfer rate is dominant near $T = T_{max}$ and becomes secondary away from this region. However, Eq. (1-78) becomes crude since the second inequality of (1-71) is not well satisfied when $T \sim T_{max}$.

The importance of this theory arises from the fact that the coherence factor is not considered negligible as was previously done. This resulted in the dramatic temperature dependences of the energy transfer that showed that this factor could not be neglected and gives many possibilities for explaining intricate temperature dependences of energy transfer that have been observed experimentally.

Apparatus

The block diagram shown in Figure 5 represents the experimental apparatus set up used for obtaining time resolved spectra and lifetimes. Two laser systems were used as excitation sources throughout this study.

The first system was an AVCO Everett model C400 pulsed nitrogen laser with an ultraviolet line output of wavelength 3371Å. The half width of the line is less than 4Å with an effective pulse width of 5 nanoseconds. The pulse rate is continuously variable from 1Hz to 100Hz.

The second system consisted of an NRG nitrogen laser and a Systems Science and Software dye laser.

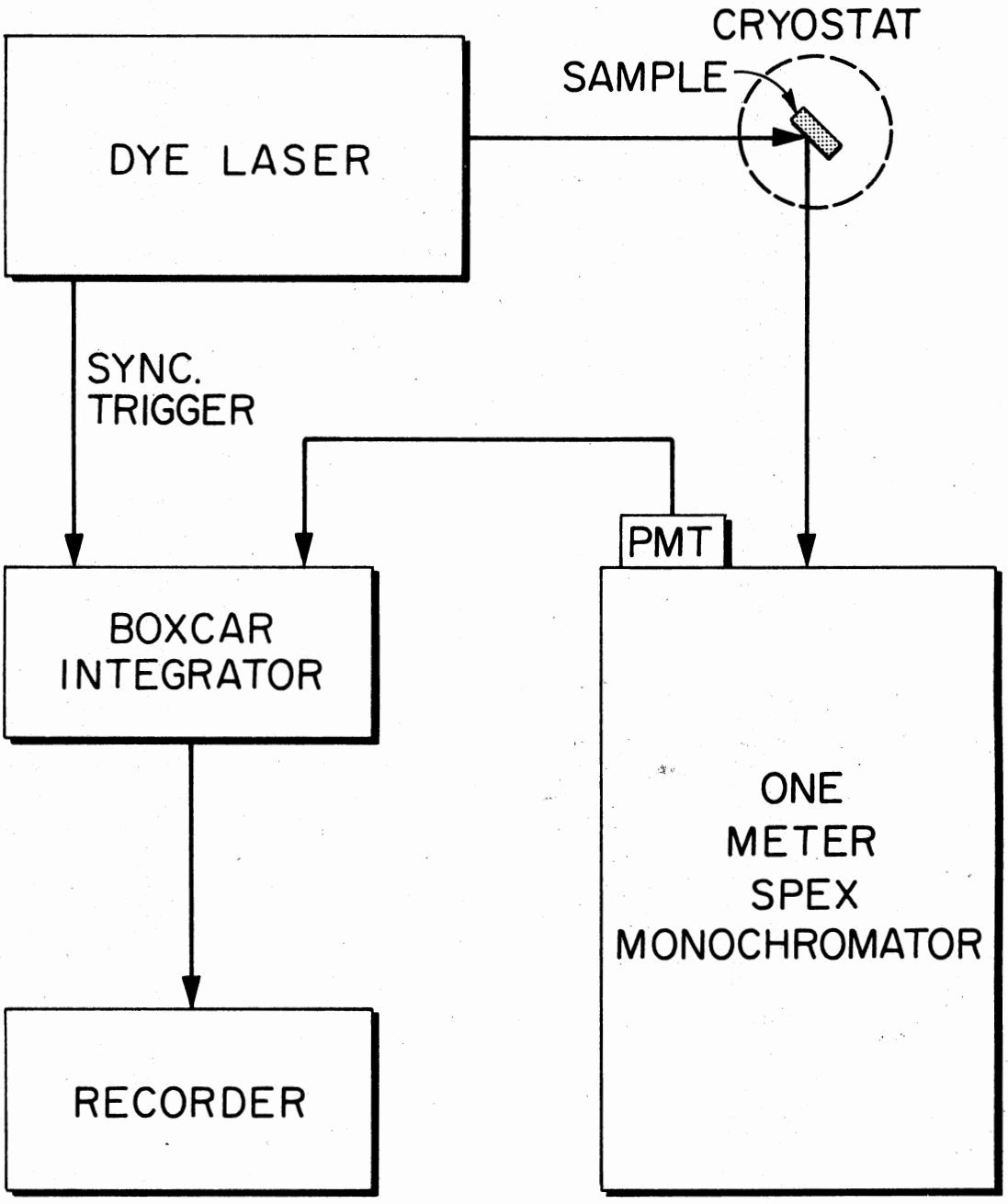

Figure 5. Time Resolved Spectroscopy Apparatus

The NRG nitrogen laser has the same line characteristics as the AVCO Everett model C400 except that the pulse width is much smaller and the duration is 8 nanoseconds and the peak power output is over one order of magnitude higher. The repetition rate was adjustable at 60, 30, 20, 15 Hz.

The NRG nitrogen laser output is focused within the flowing (for cooling purpose) dye of the S.S.S. high resolution tunable dye laser by the means of a cylindrical lens. The output line of this laser for a given dye can be tuned within an average of 300Å and by using different dyes it covers a range from 3559Å to 6818Å. The duration of the pulse is about 8 nanoseconds and the half maximum width is at minimum 0.08Å. A solution of "7-Diethylamino-4-methylcoumarin" in absolute ethyl alcohol was used as the dye and the half maximum line width of 0.1Å was obtained.

The light from one of the laser systems was focused on the sample which was mounted on the cold finger of an Air Products and Chemicals model CS-2-2 Displex Cryogenic Refrigerator. This is a closed cycle helium refrigerator with the capability of continuously varying the sample temperature from room to about $12^{o}K$. Thermal contact between the sample and the cold finger was aided by application of a small amount of Air Products Cry-con conducting grease. The temperature of the sample was measured by a chromel vs. gold-0.07 at. percent iron thermocouple.

The fluorescence light at the sample was collected at a 90^{o} angle with respect to the laser beam and was focused onto the entrance slit of a Spex one meter Czerny-Turner spectrometer model 1704. This

spectrometer has 4Å per mm dispersion with ultimate resolution of better than 0.1Å in first order. The slit width was varied depending upon the particular circumstances of the spectra. The output of the spectrometer was detected by an R.C.A. C31034 phototube with a 20 megohm load resistor which was operated at +1900 VDC. The phototube was cooled by a Products for Research Thermoelectric Refrigerated chamber at about $-20^{o}C$ in order to minimize the dark current.

The output of the phototube was processed by a Princeton Applied Research Corp. model 162 Boxcar Averager that had two model 164 Processor Modules to form a gated signal recovery system. The Averager is triggered directly from the nitrogen laser in both laser systems.

The Boxcar has a time aperture that can be continuously adjustable from 10nsec to 5msec and can be set fixed of scanned along a delay range from 5% to 100% of the range. The delay range is adjustable in a 1-2-5 sequence from 0.1 nsec to 50msec and the scanning time can be set anywhere from 10^{-2}sec to 10^{5}sec.

Lifetime Measurements

By setting the spectrometer on a fixed frequency whose lifetime we want to measure and scanning the aperture along a properly selected delay range at each given small time interval after the laser pulse, the aperture of the boxcar determines the average manitude of the fluorescence signal at the same small time interval after the laser pulse. So by allowing the aperture to scan we can record the averaged shape in time of the fluorescence signal and thus the

lifetime can be measured. In this case a variable load resistor was employed to minimize the response time of the system.

Time Resolved Spectroscopy Measurements

In this case we keep the boxcar aperture fixed at a specific time after the laser pulse and we scan the spectrometer. Then for the given small interval of time of the aperture the boxcar finds the average of the fluorescence signal at the specific time after the laser pulse. Thus by allowing the spectrometer to scan we record the fluorescence spectrum at a specific time after the pulse. The signal can then be recorded by either a strip chart recorder or an x,y Recorder.

Absorption and Excitation Measurements

The absorption spectra were obtained using a "Cary 14" spectrophotometer, using the tungsten-halogen visible light source. Ultraviolet absorption measurements were not made due to the large absorption coefficient of YVO_4 in this region.

The excitation spectra were obtained using the apparatus of Figure 6. The light source was a PEK, Inc. 150W xenon lamp, model X150. The light was focused on the entrance slit of a Spex model 1670 minimate motor driven monochromator and the selected wavelength of the output was focused on the sample. The fluorescence signal was monitored at 90^0 to the excitation path after it was chopped by a PAR model 125 mechanical chopper at a frequency of 2000Hz. The spectrometer used was the one meter Czerny-Turner that was described previously as well as the photomultiplier. The output of the

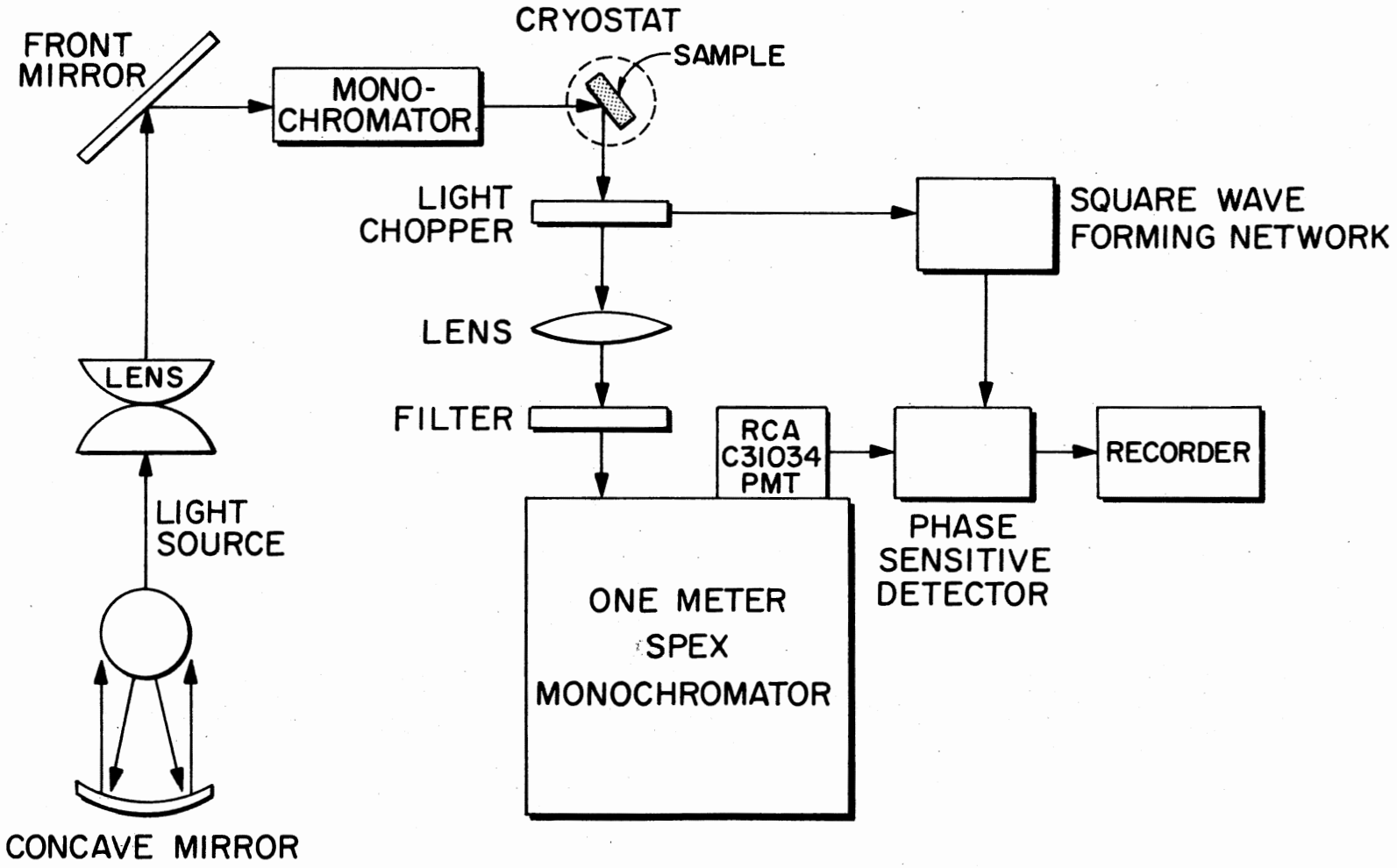

Figure 6. Block Diagram of the Continuous Fluorescence Measurement Apparatus Used for Obtaining Excitation Spectra

photomultiplier was processed by a PAR model 128 Lock-in Amplifier and the final output was recorded on a Heath model Eu-205-11 strip chart recorder. The excitation spectra were taken by keeping the monitored wavelength of the Czerny-Turner spectrometer fixed and scanning the wavelength of the excitation light via the minimate manochromator.

CHAPTER II

HOST-SENSITIZED ENERGY TRANSFER IN Eu^{3+} AND Er^{3+} DOPED YVO_4

Introduction

Yttrium vanadate crystals doped with trivalent rare earth ions are representative of an important class of laser and phosphor materials in which the excitation energy is absorbed mainly in the host material and then transferred to the activator ions. The most critical physical process involved in the practical application of these materials is the host-sensitized energy transfer. This chapter describes the results of an investigation of energy transfer in the systems $YVO_4:Eu^{3+}$ and $YVO_4:Er^{3+}$ using laser time-resolved spectroscopy (TRS) techniques.

Three samples were used for this investigation that were obtained from Raytheon, Inc. One was undoped, one contained about 1.27×10^{19} cm^{-3} europium and one with about 1.27×10^{20} cm^{-3} erbium. The experimental apparatus used to obtain the absorption, fluorescence and excitation spectra was described in the first chapter. The fluorescence lifetimes and time-resolved spectra were obtained by exciting the samples with the Avco-Everett 20kW pulsed nitrogen laser at 3371Å. The signal was processed by the PAR 162/164 boxcar averager triggered by the laser pulse. This was either set to observe the fluorescence spectra at a specific time after the laser pulse or used to scan the

fluorescence at a specific wavelength as a function of time after the laser pulse. The time resolution was of the order of 80ns.

Results and Interpretation of Undoped YVO_4 Data

The details of the optical spectra of pure yttrium vanadate were reported previously (4). The structure in the excitation spectrum was attributed to transitions between levels of the tetrahedral VO^{3-} molecular ion in a crystal field site of D_{2d} symmetry. The absorption is accompanied by a ligand-metal charge transfer. Fluorescence takes place from the lowest level of the excited state manifold after radiationless relaxation from higher excited states and lattice relaxation in the lowest level. This results in a significant Stokes shift. The crystal structure of YVO_4 is shown in Figure 7. Figure 8 shows the temperature dependence of the fluorescence decay time under laser excitation. The value of 15 μs measured at room temperature is similar to that found from broad band excitation as is the general increase in decay time as the temperature is lowered. However, the value of 495 μs measured at $12^{o}K$ is significantly greater than the value found from broadband excitation. Also, under laser excitation a rise time is observed in the pulsed fluorescence profiles which has a distinct temperature dependence as shown in Figure 8. This was not observed with broadband excitation.

The laser-excited lifetime results can be explained by assuming that fluorescence occurs from the relaxed excited state with the relaxation rate from the terminal state of the absorption transition designated as ω and the intrinsic fluorescence decay time of the level indicated by τ_T. If the temperature dependence of the observed decay time τ_H^o is due to thermally excited energy migration to radiationless

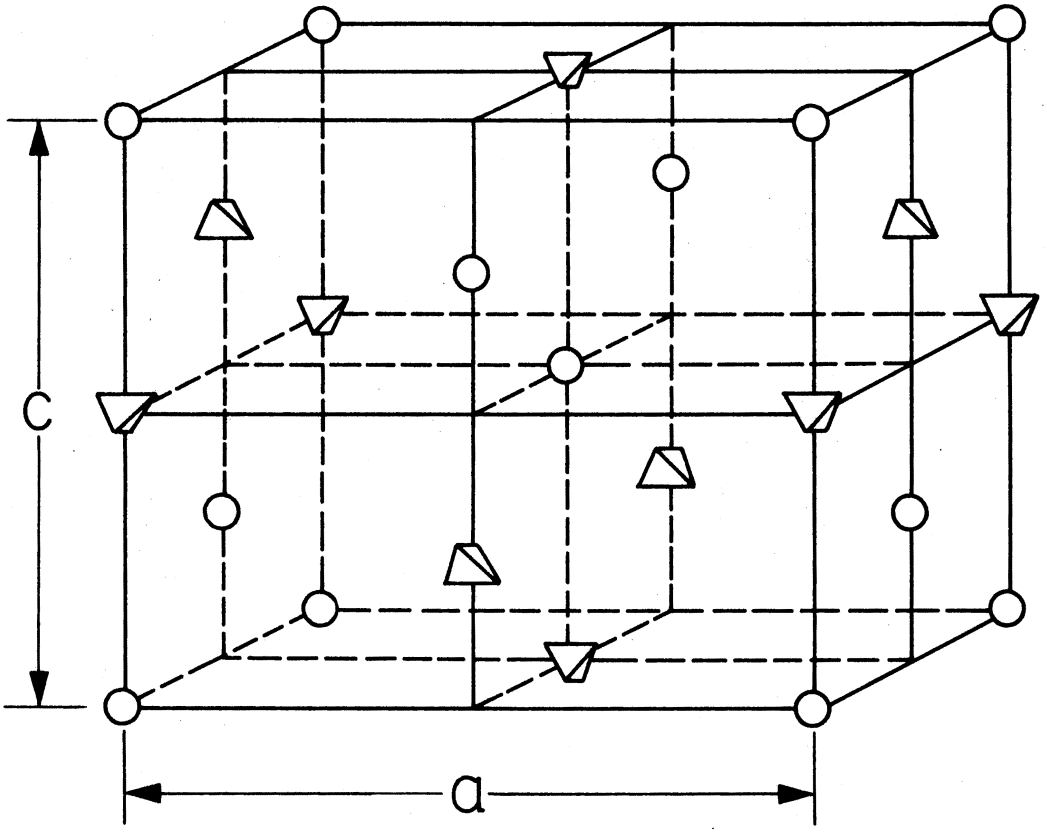

a - 7.123 Å

c - 6.291 Å

Figure 7. Zircon Structure of YVO_4

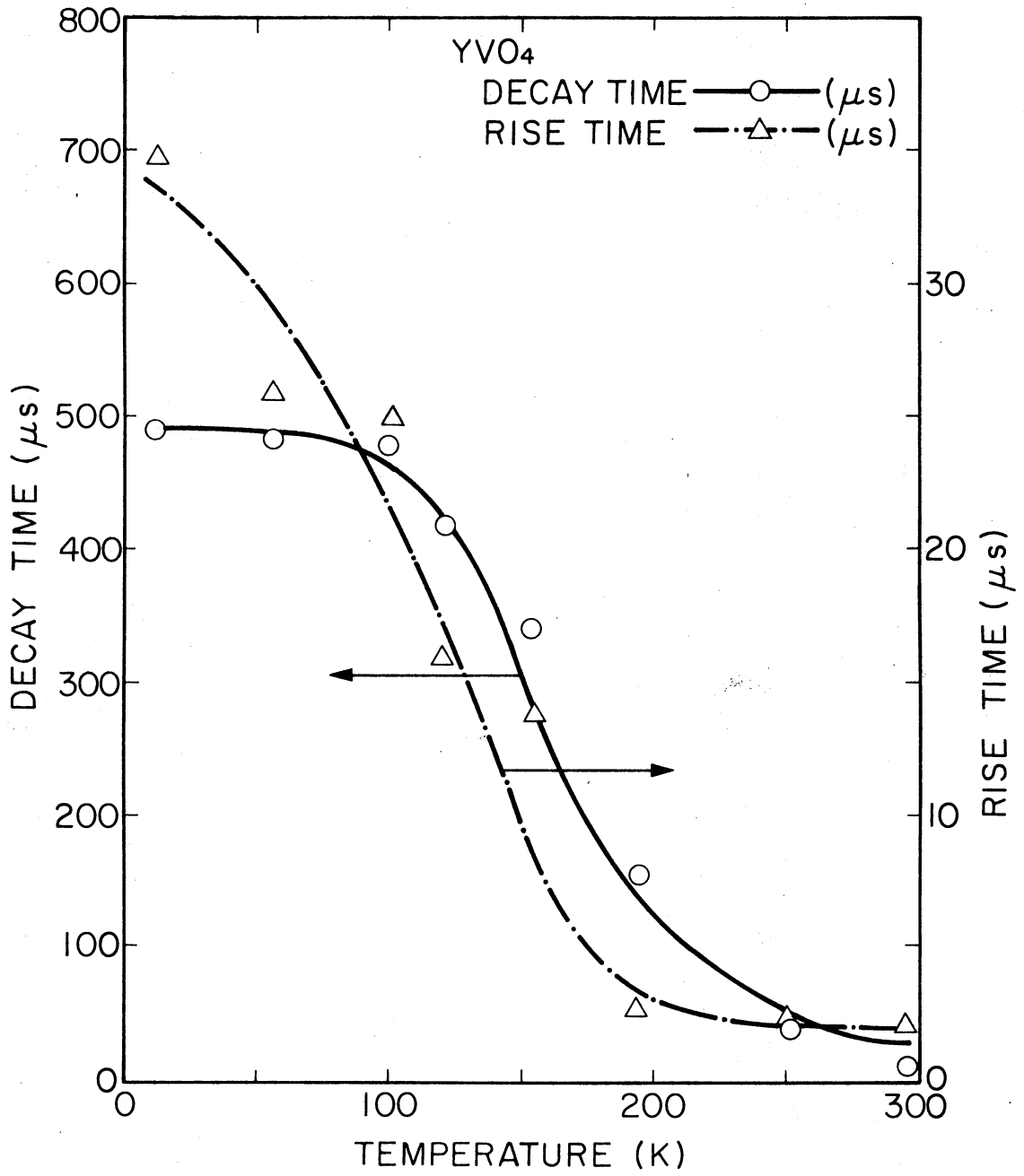

Figure 8. Temperature Dependences of the Fluorescence Decay Times and Rise Times of Undoped YVO_4 Crystals with 3371A Laser Excitation; the Solid Line is from Eq. (2-1)

quenching sites, this can be expressed theoretically as

$$(\tau_H^o)^{-1} = \tau_T^{-1} + k \exp(-\Delta E/k_B T) \qquad (2\text{-}1)$$

where ΔE is the activation energy for migration and k is the energy migration rate. In the same model the fluorescence rise time is given by

$$t_m = [\omega-(\tau_H^o)^{-1}]^{-1} \ln(\omega\tau_H^o). \qquad (2\text{-}2)$$

The solid line in Figure 8 represents the best fit to the lifetime data using Eq. (2-1). The activation energy for migration obtained from this fitting is 625.5 cm^{-1}, the migration rate is 5.0×10^5 sec^{-1}, and the intrinsic decay time of the fluorescence state is 490 μs. The temperature dependence of the fluorescence rise time can be correctly predicted by Eq. (2-1) and the value of ω at low temperatures is found to be 1.2×10^5 sec^{-1}. These parameters are summarized in Table I.

Near room temperature the observed decay time decreases somewhat faster than predicted by this simple model. This can be attributed to the onset of other radiationless decay processes which have been reported previously in this temperature region (4). The model used to interpret the laser-excited data is somewhat simpler than the model used in Reference 4 for broadband excitation. The quantitative differences in the lifetime data for the two types of excitation may be due to the selective nature of the laser absorption. Broadband sources will excite several of the vanadate excited states whereas the nitrogen laser causes absorption transitions directly to the lowest excited crystal field state of the molecular ion. If the broad fluorescence band is composed of the superposition of emission transitions of the same energies from several excited states with different Stokes shifts,

TABLE I

MODEL FITTING PARAMETERS

PARAMETER	SAMPLE		
	Undoped	Eu^{3+} ($1.27\times10^{19}cm^{-3}$)	Er^{3+} ($1.27\times10^{20}cm^{-3}$)
$R_o^{dd}(13K)(\mathring{A})$		4	2
$k(sec^{-1})$	5.0×10^5	1.0×10^4	2.2×10^5; 2.0×10^5*
$\omega(sec^{-1})$	1.2×10^5		
$W_{SA}(sec^{-1})$		2.0×10^4	2.0×10^7
$W_{10}(sec^{-1})$		1.1×10^5	
$W_X(sec^{-1})$			3.0×10^7

* The larger value is k; the smaller value is k´.

then the broadband excitation would be expected to lead to a shorter lifetime and no observed rise time since the transitions from some of the higher excited states are allowed in the VO_4^{3-} molecular ion whereas the transition from the lowest level selectively excited by the nitrogen laser is forbidden in the molecular ion and becomes allowed only through the effects of the crystal field.

Results and Interpretation of $YVO_4:Eu^{3+}$ Data

The laser excited fluorescence spectra of europium doped yttrium vanadate is similar to that observed with broadband excitation except that at high temperatures emission lines from the $^5D_1$ metastable state of Eu^{3+} can be observed. The fluorescence lifetimes are shown as a function of temperature in Figure 9 and listed in Table II. The rise times of the three transitions have similar temperature dependences to the decay times. The host vanadate fluorescence rise time decreases from 26 μs at 16°K to less than 1 μs at room temperature. In the same temperature range, the europium $^5D_0$ fluorescence rise time decreases from around 100 μs to 36 μs with a distinct peak of about 300 μs near 115°K. Similarly the $^5D_1$ fluorescence rise time decreases as temperature is raised from about 12 μs to 6 μs with a peak of about 14 μs near 150°K. The complicated temperature dependences of the $^5D_0$ and $^5D_1$ lifetimes can be attributed to the effects of energy transfer from the host. The quenching of the host lifetime in the doped sample due to energy transfer is consistent with broadband excitation results.

The TRS results obtained at very low temperature and at room temperature are shown in Figure 10 and listed in Table III, where the

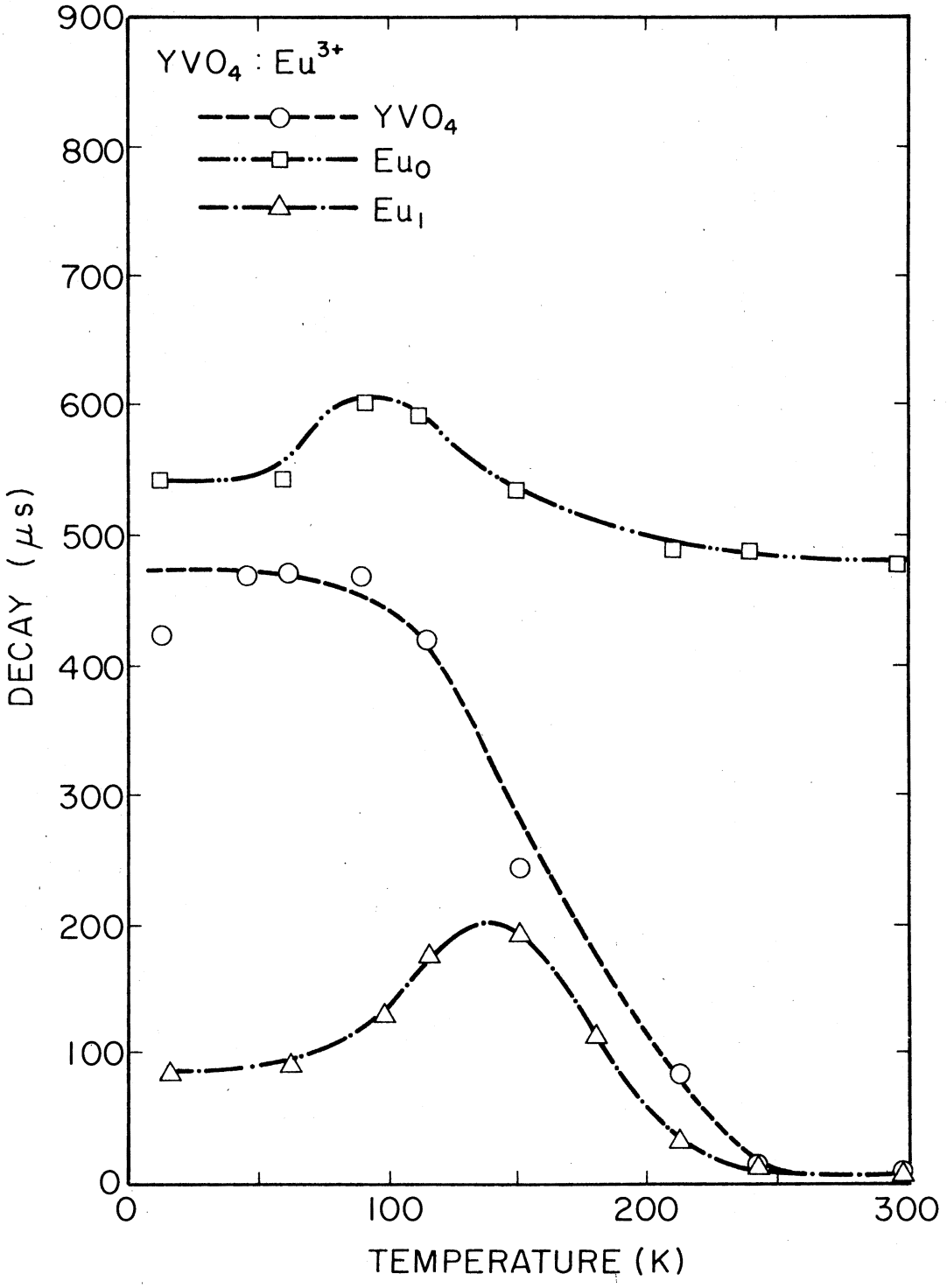

Figure 9. Temperature Dependences of the Fluorescence Decay Times in $YVO_4:Eu^{3+}$; Eu_0 and Eu_1 Indicate Emission from the $^5D_0$ and $^5D_1$ States, Respectively

TABLE II

FLUORESCENCE LIFETIMES AND RISETIME FOR $YVO_4:Eu^{3+}$ SYSTEM

	Host		$^5D_1$		$^5D_0$	
Temperature (K)	Risetime	Lifetime	Risetime	Lifetime	Risetime	Lifetime
16	26	462	12	87	85	546
61	22	470	13	93	90	548
98	35	486	12.5	130	100	605
115	6	423	6.4	179	300	596
150	4.5	243	14	193	275	539.2
210	1.9	86	14.5	34	90	491
240	1.7	13.8	9	17.5	57	490
300	--	4.3	6.2	8.5	36	478

Lifetimes and risetimes are given in (μs)

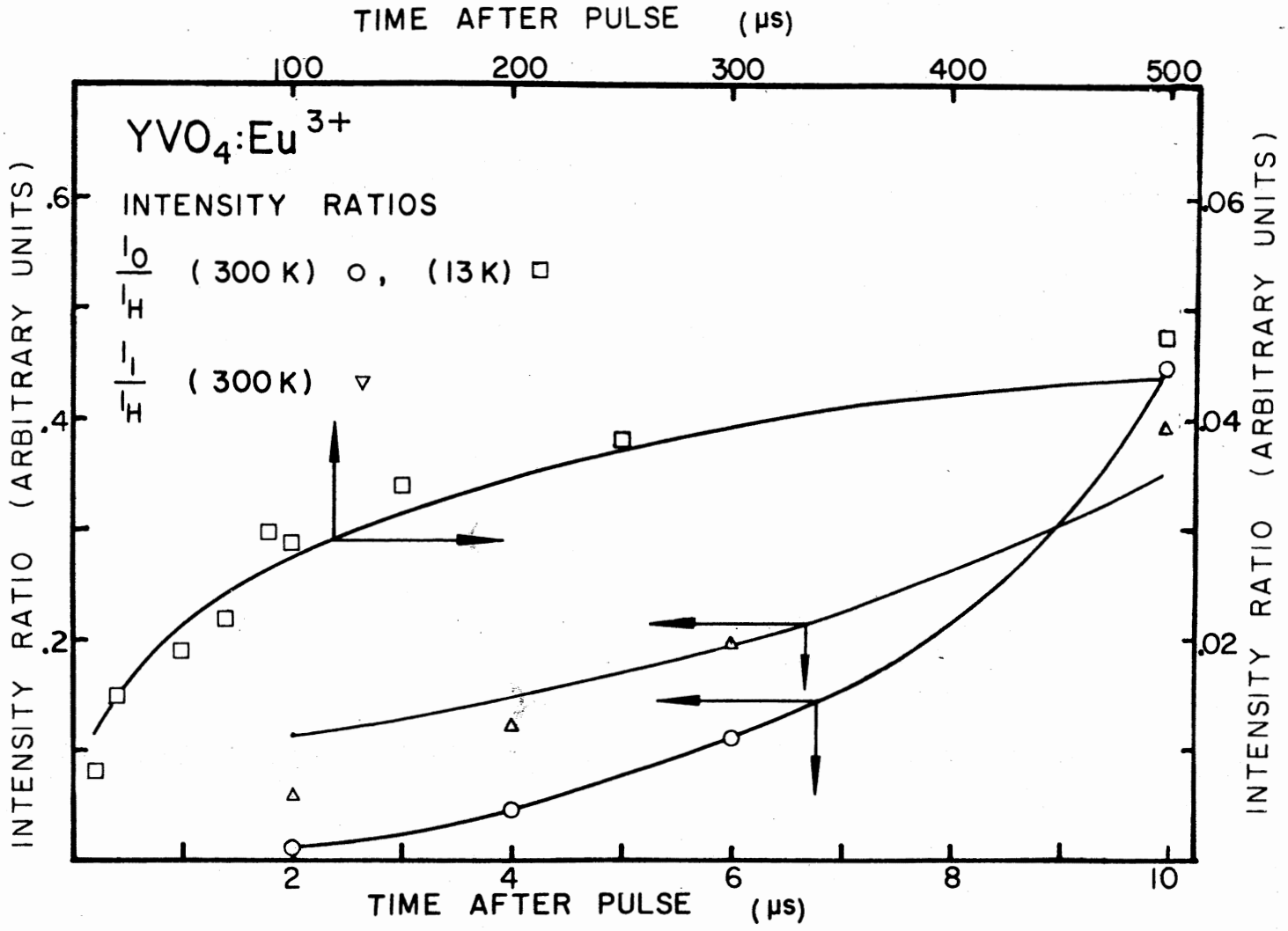

Figure 10. Laser TRS Results for $YVO_4:Eu^{3+}$ Crystals with 1.27×10^{19} cm^{-3} Eu^{3+}; See Text for Explanation of Theoretical Lines

TABLE III

FLUORESCENCE INTENSITY RATIOS AT DIFFERENT TIMES AFTER THE LASER PULSE

Time After Pulse*	I_{0/I_H}	I_{1/I_H}	$(I_0+I_1)/I_H$	$- I_{1/I_0}$
		16K		
6	0.000	-	-	-
10	0.000	-	-	-
20	0.015	-	-	-
50	0.019	-	-	-
70	0.022	-	-	-
90	0.030	-	-	-
100	0.029	-	-	-
150	0.034	-	-	-
250	0.038	-	-	-
500	0.047	-	-	-
1000	0.044	-	-	-
		17K		
2	0.000	0.000	0.000	0.000
6	0.004	0.010	0.014	2.500
10	0.011	0.022	0.033	2.000
25	0.060	0.039	0.099	0.650
50	0.323	0.080	0.404	0.250
		300K		
2	0.011	0.055	0.067	5.000
4	0.044	0.122	0.166	2.772
6	0.113	0.187	0.301	1.654
10	0.444	0.398	0.842	0.896

* Time after the pulse is given in microseconds.

I_0 is the intensity of $^5D_0$ and I_1 is the intensity of $^5D_1$.

integrated fluorescence intensity of the europium emission divided by that of the host emission is plotted as a function of time after the laser pulse. At room temperature separate plots are made for transitions originating on the $^5D_0$ and the $^5D_1$ levels of Eu^{3+}. At low temperatures only the former can be observed with any degree of accuracy.

These results can be explained by a model in which the excited states of the host vanadate molecular ions are treated as localized excitons which are self-trapped due to lattice relaxation at low temperature and undergo thermally activated hopping migration at high temperature. The activator impurity ions distort the surrounding vanadate ions creating activator-induced host traps which can trap the excitons. The trapped excitons then transfer their energy to the nearby activators. The energy levels and transition rates are shown schematically in Figure 11. W is the rate of creation of host excitons, n_H is the concentration of excitons and β_H is their fluorescence decay rate. k represents the rate of exciton migration and trapping at activator-induced host traps. n_{XA} is the concentration of excited traps and W_{SA} is the energy transfer rate from trap to nearest neighbor activator. It is assumed that transfer occurs preferentially to the $^5D_1$ state which has a concentration n_1 and can decay to the ground state with a rate β_1 or to the $^5D_0$ state with a rate W_{10}. The latter state has a population of n_0 and a fluorescence decay rate β_0. The rate equations for the excited state populations are

$$dn_H/dt = W-\beta_H-kn_H \qquad (2\text{-}3)$$

$$dn_{XA}/dt = kn_H-W_{SA}n_{XA} \qquad (2\text{-}4)$$

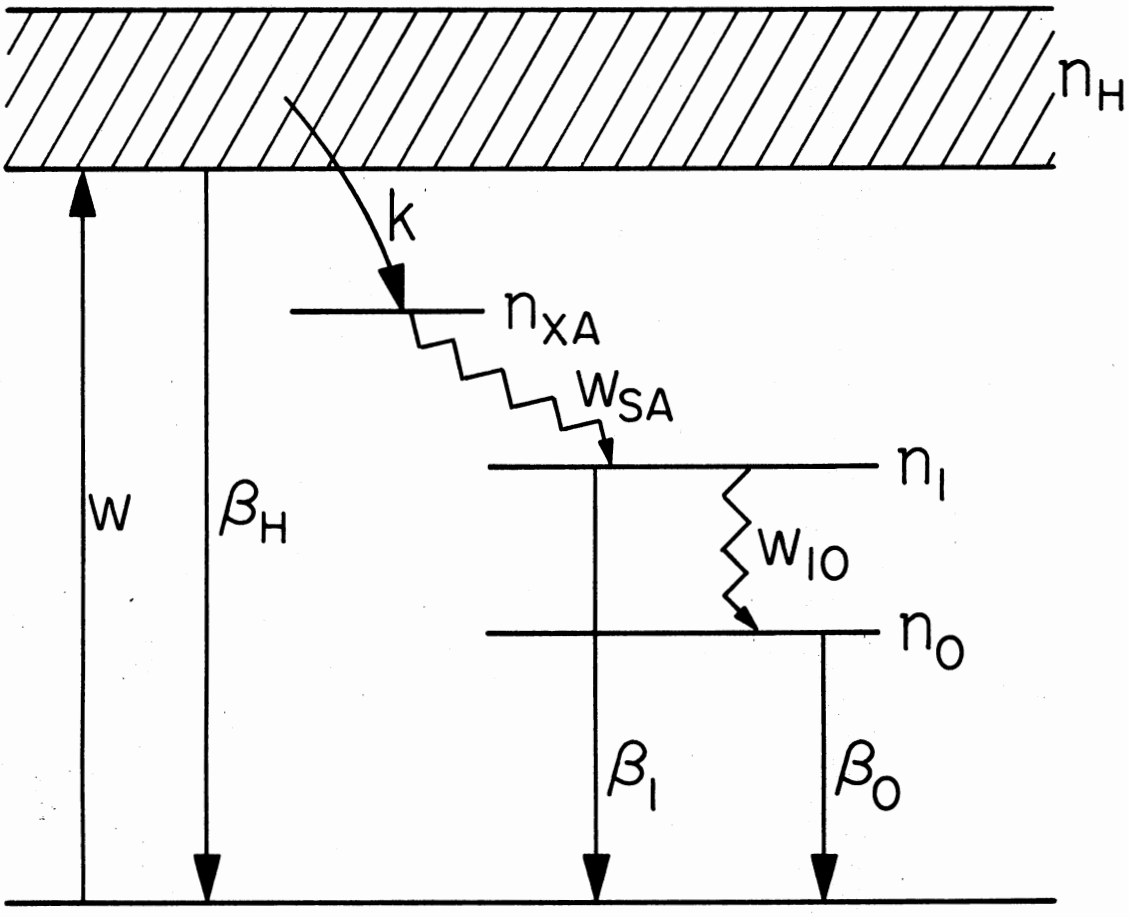

Figure 11. Model for Host-Sensitized Energy Transfer in $YVO_4:Eu^{3+}$

$$dn_1/dt = W_{SA}n_{XA} - (W_{10}+\beta_1)n_1 \tag{2-5}$$

$$dn_0/dt = W_{10}n_1 - \beta_0 n_0. \tag{2-6}$$

These can be solved assuming a delta function excitation pulse to obtain the required fluorescence intensity ratios,

$$\frac{I_1}{I_H} = \left[\frac{\beta_1' k}{\beta_H'} \frac{W_{SA}}{W_{SA}-\tau_H^{-1}}\right] \left\{\frac{1}{\tau_1^{-1}-\tau_H^{-1}} + \frac{1}{W_{SA}-\tau_1^{-1}} e^{-(W_{SA}-\tau_H^{-1})t} + \frac{W_{SA}-\tau_H^{-1}}{(\tau_1^{-1}-W_{SA})(\tau_1^{-1}-\tau_H^{-1})} e^{-(\tau_1^{-1}-\tau_H^{-1})t}\right\} \tag{2-7}$$

$$\frac{I_0}{I_H} = \left[\frac{\beta_0' k}{\beta_H'} \frac{W_{10}W_{SA}}{W_{SA}-\tau_H^{-1}}\right] \left\{\frac{1-e^{-(\tau_0^{-1}-\tau_H^{-1})t}}{(\tau_1^{-1}-\tau_H^{-1})(\tau_0^{-1}-\tau_H^{-1})} + \frac{e^{-(W_{SA}-\tau_H^{-1})t} - e^{-(\tau_0^{-1}-\tau_H^{-1})t}}{(W_{SA}-\tau_1^{-1})(\tau_0^{-1}-W_{SA})} + \frac{e^{-(\tau_1^{-1}-\tau_H^{-1})t} - e^{-(\tau_0^{-1}-\tau_H^{-1})t}}{(\tau_1^{-1}-W_{SA})(\tau_1^{-1}-\tau_H^{-1})(\tau_0^{-1}-\tau_1^{-1})}\right\} \tag{2-8}$$

where the prime indicates radiative decay rates and the lifetimes which can be measured have been used in place of the appropriate combinations of decay rates. The solid lines in Figure 10 represent the best fit to the room temperature data using Eqs. (2-7) and (2-8) with W_{SA} and the

factors in square brackets treated as adjustable parameters. If the constant lifetimes which are approached at low temperatures are taken as good approximations to the radiative decay times, k and W_{10} can also be determined. These parameters are summarized in Table I.

At low temperatures the model can be simplified greatly since no exciton migration is present and all fluorescence occurs from the $^5D_0$ level. Thus the host excited states are self-trapped excitons which can fluoresce or transfer their energy in a single step process to the nearest activator which can effectively be treated as having only one excited state. If the transfer occurs through electric dipole-dipole interaction, the equation derived to describe the TRS data is

$$I_0(t)/I_H(t) = (\beta_0'/\beta_H') \left\{\frac{\omega(t)[\beta_H+\omega(t)]}{[\beta_H+\omega(t)-\beta_A]^2}\right\} \left\{e^{-[\beta_A-\beta_H-\omega(t)]t}-1\right\} \tag{2-9}$$

with

$$\omega(t) = \frac{4}{3}\pi^{3/2}R_0^3C_A(\tau_H^o t)^{-1/2} \tag{2-10}$$

where R_0 is the critical interaction distance, C_A is the concentration of Eu^{3+}, and τ_H^o is the host fluorescence decay time in the undoped sample. The solid line in Figure 10 represents the best fit to the low temperature data using Eq. (2-9) and treating R_0 as an adjustable parameter. The quantitative results are listed in Table I.

The predictions of the model assumed here give an excellent fit to the data involving the $^5D_0$ europium emission at both high and low temperatures. The fit to the $^5D_1$ TRS data is not as good. This may

either be due to the poorer accuracy of these data or to the fact that the physical situation is more complicated than that considered in the model. The high temperature exciton transfer rate and trap to activator transfer rate and the low temperature value of R_0 reported in Table I are all consistent with the values found from intensity and lifetime quenching investigations (4). The radiationless relaxation rate between the excited states of Eu^{3+} is consistent with that reported from other investigations (5). Also the complicated temperature dependence of the $^5D_1$ fluorescence decay time can be explained by this model which describes the emission as the sum of three exponentials, one having the decay time of the host which dominates at high temperatures, and one having the intrinsic decay time of the $^5D_1$ level which dominates at low temperatures.

Results and Interpretation of $YVO_4:Er^{3+}$ Data

The absorption spectrum of erbium doped yttrium vanadate is shown in Figure 12 and the fluorescence spectra are shown in Figure 13. The sharp line spectra are similar to those observed for Er^{3+} in other hosts (6). Again fluorescence from two metastable states can be observed at room temperature while only transitions originating from the lowest excited state remain. It is well known that trivalent erbium also has numerous efficient emission lines in the near infrared region of the spectrum not investigated here (6).

Figure 14 shows the fluorescence lifetimes obtained at different temperatures and these are listed in Table IV. The observed fluorescence

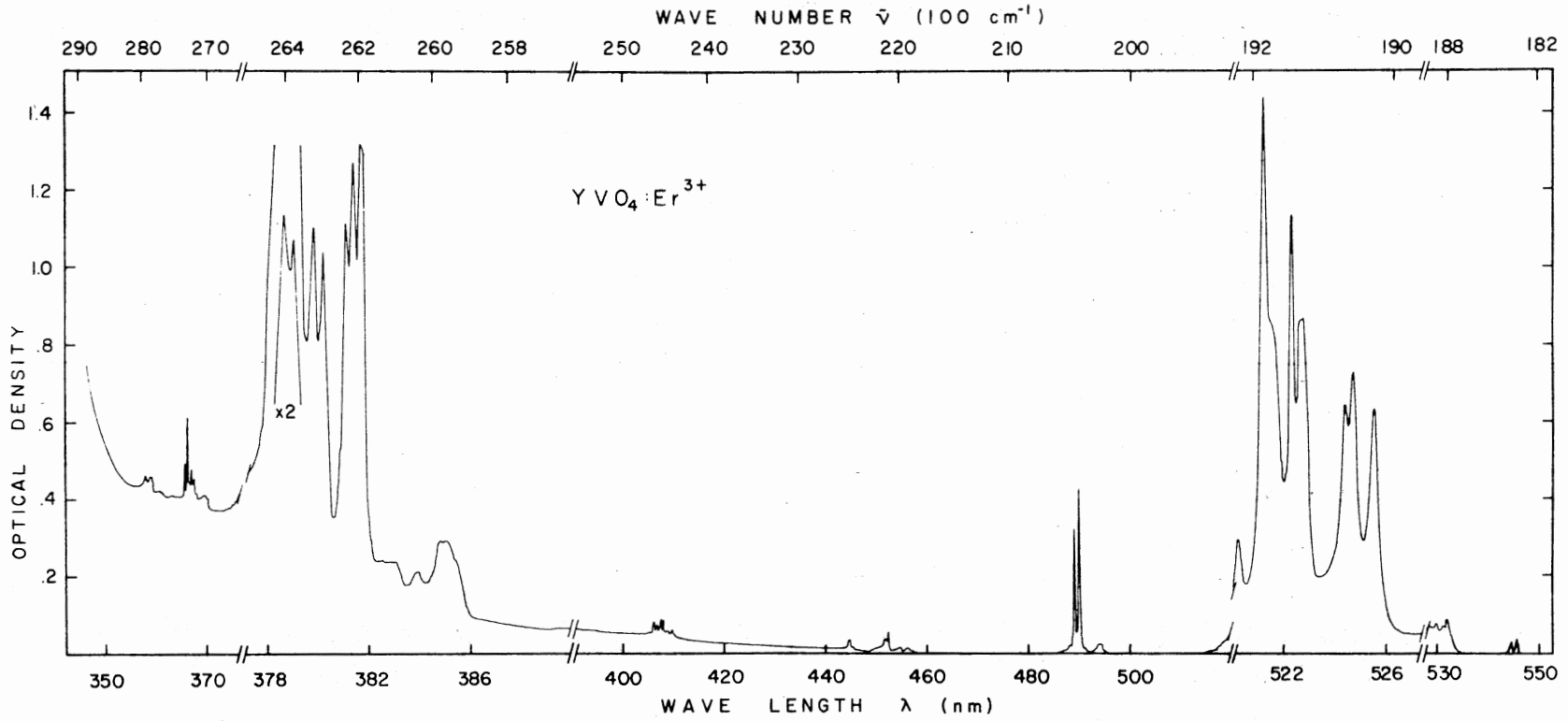

Figure 12. Room Temperature Absorption Spectrum of $YVO_4:Er^{3+}$ Crystal with 1.27×10^{20} cm^{-3} Er^{3+}; Sample Thickness is 0.9 mm

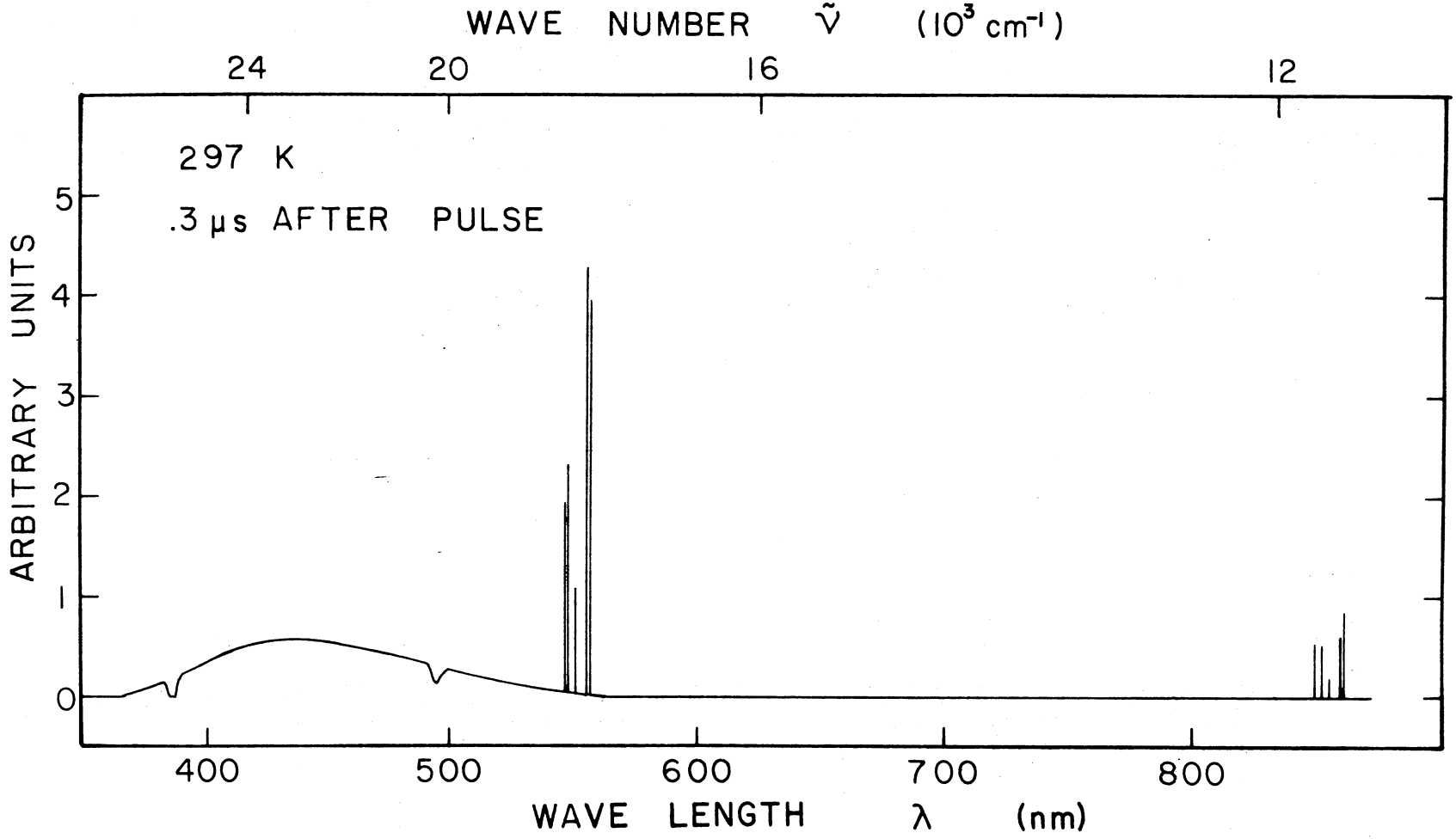

Figure 13a. Fluorescence Spectrum of $YVO_4:Er^{3+}$ with 1.27×10^{20} cm^{-3} Er^{3+} Taken at Room Temperature

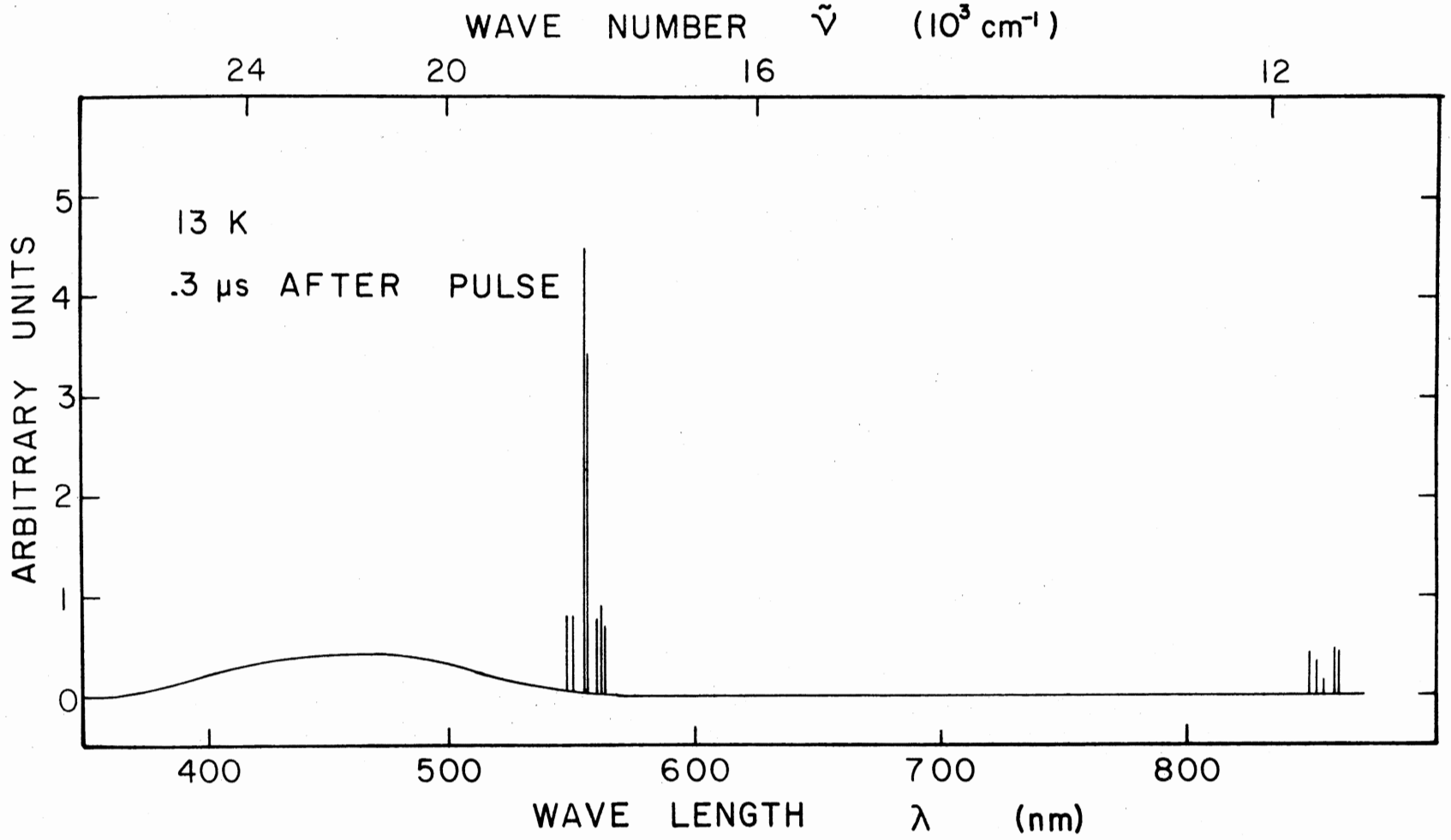

Figure 13b. Fluorescence Spectrum of $YVO_4:Er^{3+}$ with 1.27×10^{20} cm^{-3} Er^{3+} Taken at 13°K

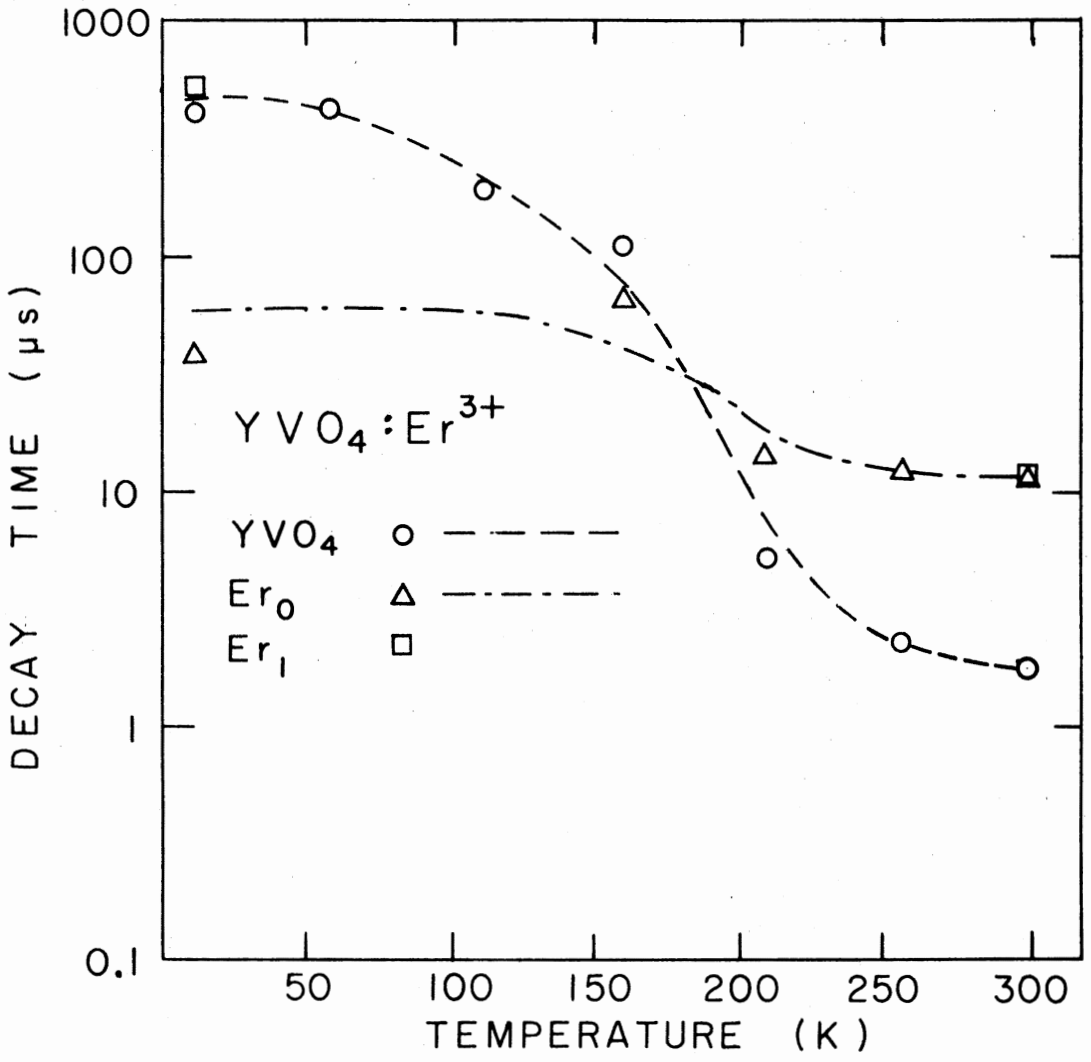

Figure 14. Temperature Dependences of the Fluorescence Decay Times in $YVO_4:Er^{3+}$; Er_0 and Er_1 Indicate Emission from the $^4S_{3/2}$ and $^2H_{11/2}$ States, Respectively

TABLE IV

LIFETIMES AND RISETIMES OF THE SYSTEM $YVO_4:Er^{3+}$ AT DIFFERENT TEMPERATURES

	Host		$^5D_1$ Emission		$^4S_{3/2}$ $^5D_0$ Emission	
Temperature (K)	Risetime	Lifetime	Risetime	Lifetime	Risetime	Lifetime
12	.16	414	.150	521	3	38
58	.60	434	--	--	--	--
113	.75	191	--	--	--	--
161	.90	112	--	--	6.5	67
210	.94	5	--	--	4.5	14
256	.43	2.3	--	--	2.4	12.8
300	.25	.53	.5	11.2	.85	11.4

Lifetimes and risetimes are given in (μs)

rise times in this case are all less than 1 μs, and difficult to measure with any degree of accuracy. The erbium lifetimes decrease slightly due to radiationless transitions as temperature is raised. The temperature dependence of the vanadate fluorescence lifetime is similar to that seen in the europium doped sample. Figure 15 shows the temperature dependences of the integrated fluorescence intensity and lifetime ratios which are directly related to the rate of energy transfer. These are listed in Table V. They both decrease slightly as the temperature is raised from 13°K to about 65°K which can be attributed to the thermal activation of self-trapped excitons which decreases the amount of single step energy transfer. Above about 150°K both curves exhibit a sharp exponential increase with temperature as the excitons become mobile enough to migrate to activators. The solid lines represent the best fit to the data which is obtained with an activation energy of about 1,000 cm^{-1}. This is qualitatively consistent with the results obtained on the europium doped sample. The difference in magnitudes for the intensity and lifetime data can be attributed to the differences in quantum efficiencies of the Er^{3+} and host emissions.

Results of TRS investigations are shown in Figure 16 for both room temperature and 13°K and listed in Table VI. The model used to interpret these data is shown in Figure 17. The rate parameters and excited state populations are similar to those in Figure 11. In this model back transfer from traps to the host band is included as is direct transfer from the host to both the metastable states of the activators. It is unnecessary to include radiationless relaxation

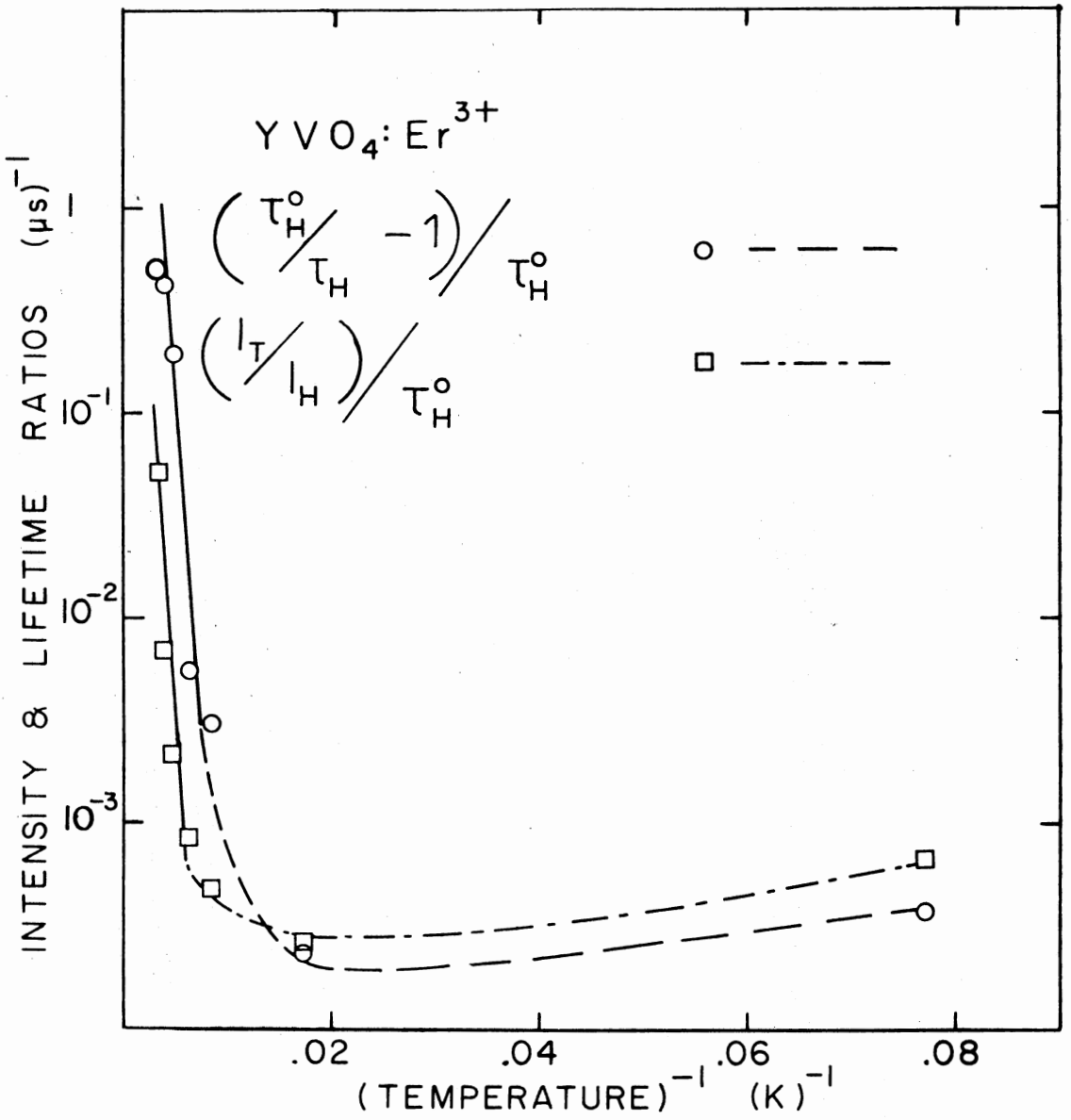

Figure 15. Temperature Dependences of the Fluorescence Intensity and Lifetime Ratios in $YVO_4:Er^{3+}$; I_T Represents the Sum of All the Er^{3+} Transitions; the Intensities are Measured at 0.7 μs After the Laser Pulse; the Solid Lines are Given by Exp $[1{,}000\ cm^{-1}/(k_BT)]$

TABLE V

FLUORESCENCE INTENSITIES AND LIFETIME RATIOS OF $YVO_4:Er^{3+}$ AT DIFFERENT TEMPERATURES

Temperature (K)	$(I_{T/I_H})/\tau_H^o$ *	$(\tau_H^o/\tau_H - 1)/\tau_H^o$ **
13	6.71×10^{-14}	3.75×10^{-4}
58	2.42×10^{-4}	2.34×10^{-4}
113	4.89×10^{-4}	3.01×10^{-3}
161	8.4×10^{-4}	5.60×10^{-3}
210	2.07×10^{-3}	1.9×10^{-1}
256	6.87×10^{-3}	4.1×10^{-1}
300	5.03×10^{-2}	1.8

* I_T is the total intensity of the $^5D_1$ and $^5D_0$

** τ_H^o is the lifetime of the YVO_4 when undoped and

τ_H is the lifetime of the YVO_4 when doped

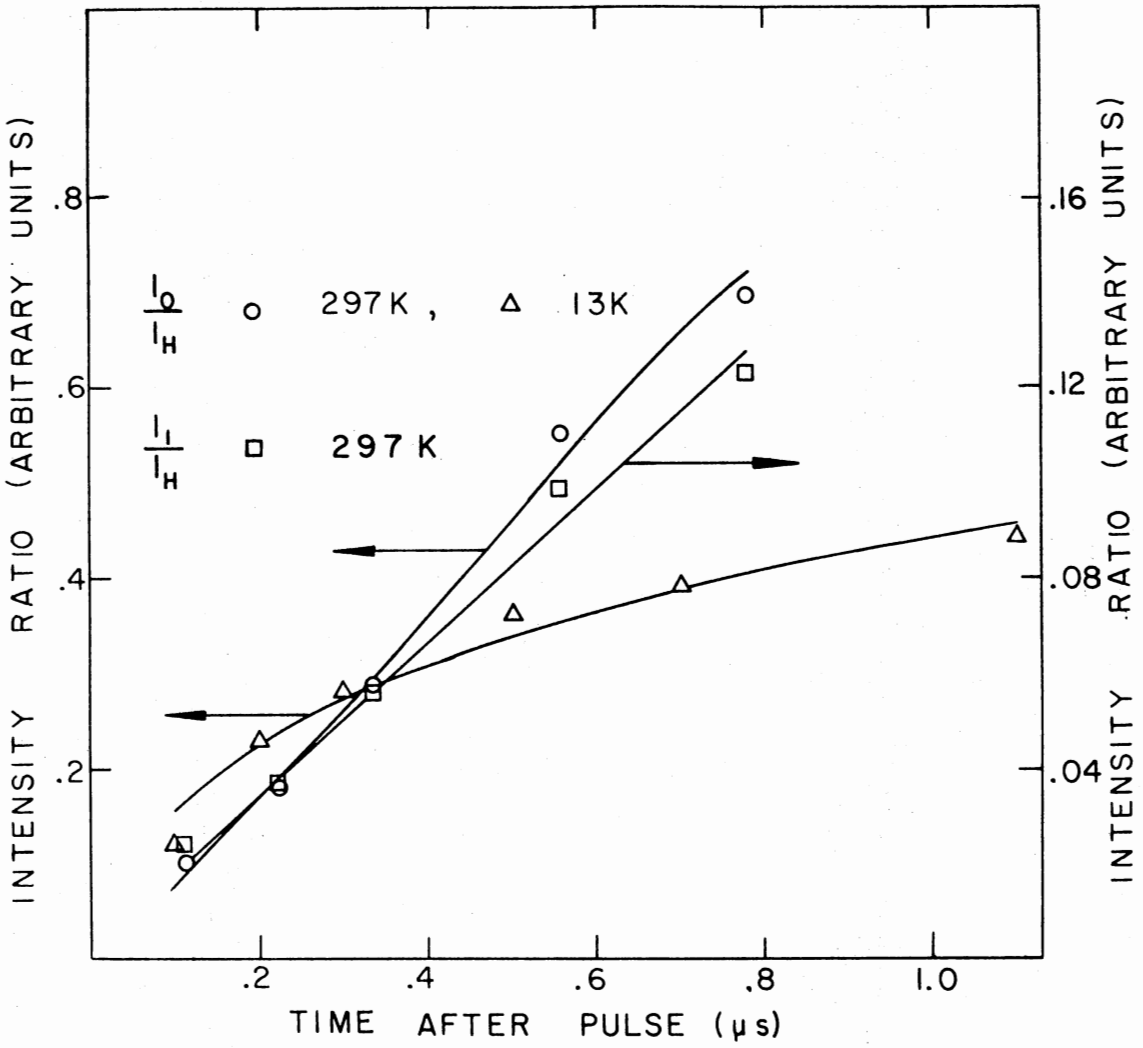

Figure 16. Laser TRS Results for $YVO_4:Er^{3+}$ Crystals with 1.27×10^{20} cm^{-3} Er^{3+}

TABLE VI

FLUORESCENCE INTENSITY RATIOS AT DIFFERENT TIMES AFTER THE LASER PULSE AT ROOM TEMPERATURE IN $YVO_4:Er^{3+}$

Time A.P. (μs)	I_{0/I_H}	I_{1/I_H}
100	.103	.024
200	.177	.037
300	.288	.056
500	.556	.099
700	.698	.123
1100	--	--

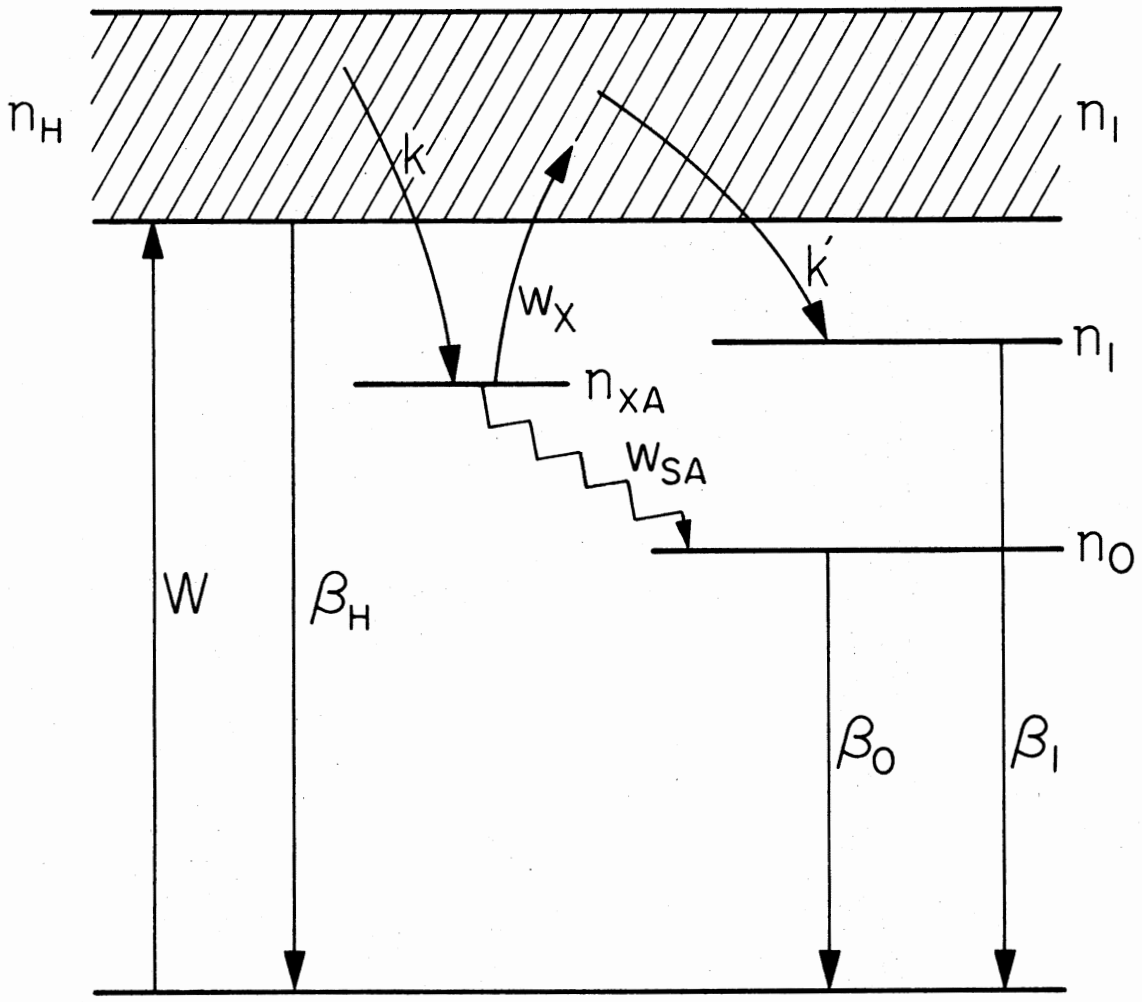

Figure 17. Model for Host-Sensitized Energy Transfer in $YVO_4:Er^{3+}$

between the two excited metastable states of the activator in order to fit the data in this case. The rate equations for the excited state populations are

$$dn_H/dt = W - \beta_H n_H - (k+k')n_H + W_X n_{XA} \tag{2-11}$$

$$dn_{XA}/dt = kn_H - W_{SA} n_{XA} - W_X n_{XA} \tag{2-12}$$

$$dn_1/dt = k' n_H - \beta_1 n_1 \tag{2-13}$$

$$dn_o/dt = W_{SA} n_{XA} - \beta_o n_o . \tag{2-14}$$

These can be solved assuming a delta function excitation pulse to obtain the required fluorescence intensity ratios,

$$\frac{I_0}{I_H} = \left[\frac{\beta_0' k}{\beta_H'} \frac{W_{SA}}{(W_{SA}+W_X)}\right] \left\{\tau_0(e^{-t/\tau_0}-1) + \frac{1}{\tau_0^{-1}-W_{SA}-W_X} (e^{-(W_{SA}+W_X)t} - e^{-t/\tau_0})\right\} \tag{2-15}$$

$$\frac{I_1}{I_H} = \left[\frac{\beta_1' k'}{\beta_H'}\right] \left\{\tau_1(1-e^{-t/\tau_1})\right\} \tag{2-16}$$

here again the prime indicates radiative decay rates, while the lifetimes which can be measured have been used in place of the appropriate combinations of decay rates. The solid lines in Figure 16 represent the best fit to the room temperature data using Eqs. (2-15) and (2-16) with W_{SA}, W_X, and the factors in square brackets treated as adjustable parameters. As before, the constant lifetimes approached at low temperatures are taken as good approximations to the radiative decay times

in order to determine k and k´. The parameters for this case are also summarized in Table I.

The model used to interpret the low temperature data is the same as that used in the previous section. The solid line in Figure 16 represents the best fit to the low temperature data using Eq. (2-9) and treating R_0 as an adjustable parameter. The result is given in Table I. The good fits to the data in Figure 16 indicate the validity of the assumed model. Numerous other models were investigated, but none were found to be consistent with the observed results.

Discussion

The critical interaction distance between randomly distributed self-trapped excitons and activators at low temperatures, can be predicted theoretically for electric dipole-dipole interaction (4). It is found to be 4Å and 2Å for the europium and erbium activators respectively. These are in close agreement with the values of R_0 found experimentally. They indicate very weak energy transfer at these temperatures with the larger value for Eu^{3+} being due to a somewhat larger spectral overlap with the vanadate emission.

The data obtained on the quenching of the fluorescence intensity and lifetimes indicate an exponential increase in energy transfer with increasing temperature for all three samples investigated. The fact that the activation energies for the temperature dependences are different in each case indicates that the trapping process at activators has an exponential temperature dependence associated with it as well as the thermal activation of exciton hopping. This is not surprising

since emission and absorption of phonons may be involved for the conservation of energy.

In the analysis of TRS data the parameters characterizing exciton migration up to an activator trapping region and the final trap-to-activator transfer step are determined separately. In the simplest model for exciton diffusion where the exciton is trapped on the first visit to any trapping site it happens to encounter, the energy transfer rate to the traps is given by (7)

$$k = 4\pi D R_A C_A \qquad (2\text{-}17)$$

where D is the diffusion coefficient, R_A is the trapping radius, and C_A is the concentration of activators. The trapping radius of an activator is determined by the differences in size and electronic structure between it and the host ion it replaces. In this case the activators substitute for Y^{3+} ions which have a radius of 0.93Å. The ionic radius of Eu^{3+} is 1.03Å and that of Er^{3+} is 0.96Å. This indicates a slightly larger size mismatch for the europium activators although the mismatch is not very large in either case. Because of this, a reasonable approximation to the trapping radius is the distance from the activator ions to the nearest neighbor vanadate molecular ion which is 3.15Å. Using this value in Eq. (2-17) predicts a diffusion coefficient of $D = 2.0 \times 10^{-4}$ cm^2 sec^{-1} for Eu^{3+} and 4.4×10^{-9} cm^2 sec^{-1} for Er^{3+} activators is predicted. (In treating the Er^{3+} case, k and k´ have been added to gether which is justified by the fact that the diffusion contribution to these rate parameters is identical and they differ only in the number of activators which accept the energy in the higher metastable state as opposed to the lower level.)

If the exciton migration is approximated as a nearest neighbor hopping on a simple cubic lattice, the diffusion length and hopping time are given by

$$\ell = \sqrt{2D\tau_H^o} \tag{2-18}$$

$$t_H = \alpha^2/6D \tag{2-19}$$

where α is the lattice spacing between VO_3^{3-} ions which is 4.75Å in YVO_4 crystals. With the diffusion coefficient found above, these equations give values of $\ell = 2.4 \times 10^{-7}$ and 3.6×10^{-7} cm and $t_H = 1.9 \times 10^{-7}$ and 8.5×10^{-8} sec for Eu^{3+} and Er^{3+} activators, respectively. The number of steps in the exciton's random walk can be estimated from the expression

$$n = \tau_H^o/t_H \tag{2-20}$$

and is found to be 79 for Eu^{3+} and 176 for Er^{3+} activators.

These exciton migration parameters are summarized in Table VII. They should be expected to be independent of the type of activator ion which is essentially true for the Eu^{3+} and Er^{3+} doped samples considering the approximate nature of the simple diffusion model used to interpret the results.

Theoretical estimates for the single step rates for exciton hopping and trap to activator energy transfer can be obtained either from the expressions for electric dipole-dipole or exchange interactions. The predictions of electric dipole-dipole interaction, are found to be inconsistent with the observed values. The transfer rate for exchange interaction is given by

$$W(ex) = (\tau_S^o)^{-1}\exp[\gamma(1-R/R_0')]. \tag{2-21}$$

TABLE VII

EXCITON MIGRATION AND TRAPPING PARAMETERS

PARAMETER	Eu^{3+} ($1.27 \times 10^{19} cm^{-3}$)	Er^{3+} ($1.27 \times 10^{20} cm^{-3}$)
D ($cm^2 sec^{-1}$)	2.0×10^{-9}	4.4×10^{-9}
ℓ (cm)	2.4×10^{-7}	3.6×10^{-7}
t_H (sec)	1.9×10^{-7}	8.5×10^{-8}
n	79	176
t_{diff} (sec)	1.0×10^{-4}	2.4×10^{-6}
t_{trap} (sec)	5.0×10^{-5}	4.9×10^{-8}
C (A)	5	9

Here $\gamma = 2R_0'/L$, where L is an effective Bohr radius and R_0' is the critical interaction distance given by

$$R_0' = (L/2)\ \ell n\ [(2\pi\tau_S^o/\ )\ K^2\Omega]. \qquad (2\text{-}22)$$

Ω is the overlap integral of the absorption spectrum of the activator and the emission spectrum of the sensitizer and K involves the wave function overlap which generally cannot be determined easily. Exchange interaction predicts the observed exciton hopping times for R_0' of the order of 7Å assuming a nearest neighbor vanadate separation of 4.75Å and a value of L equal to half the yttrium-oxygen spacing, $\simeq$ 1Å. A similar analysis gives the observed values for W_{SA} for R_0' (Eu) = 2.5Å and R_0' (Er) = 6.0Å assuming a nearest neighbor vanadate-activator distance of 3.15Å. Since K is unknown for these cases it is not possible to derive values of R_0' theoretically. However, the values obtained in this analysis appear to be physically reasonable.

Table VII also lists the reciprocal of the measured rate parameters for migration and trapping as the diffusion time t_{diff} and trapping time t_{trap}, respectively. For both samples the trapping time is found to be shorter than the diffusion time which is the case of "diffusion limited energy transfer." However, for a sample with europium activators of concentration equal to that of the erbium doped sample the diffusion time would be shorter than the trapping time giving the case of "trap limited energy transfer" as found previously (4).

An alternate way of interpreting the migration and trapping characteristics is through the generalized random walk theory developed by Soos and Powell (7). This model has recently been used to explain

energy transfer in cathodoluminescence of this type of phosphor material (8). In this theory the energy transfer rate determined experimentally is given by

$$k = C_a V_m C(A) t_H^{-1} \tag{2-23}$$

where V_m is the volume per molecule and C(A) is the capacity of the random walk. The latter quantity is defined as the rate at which new sites are sampled by the exciton per step in the limit of many steps. This can be calculated theoretically for simple cases and has been found emperically from TRS measurements for several systems of doped aromatic hydrocarbon crystals (9). It can be directly related to the size and shape of the trapping region surrounding the activators, and to the annisotropy of the random walk. The data discussed above yield values of 9 and 5 for the capacities of the erbium and europium doped samples, respectively. For a simple cubic lattice these values would correspond to trapping regions extending out to approximately third nearest neighbors around each activator (7).

CHAPTER III

LASER SITE SELECTION INVESTIGATION OF Eu^{3+} IONS IN YVO_4 CRYSTALS

The recently introduced method of using narrow band tunable dye lasers as excitation sources provides a very useful tool in the investigation of energy transfer. The fact that the line width of such laser sources together with the ability of choosing the wavelength of this line within a very broad range provides one with a light source capable of exciting very closely spaced energy levels, such as levels of ions of the same type but located in different electronic environments.

In a case that the concentration of active ions in a host crystal is high enough as to permit ion-ion interaction, energy migration may occur among these ions that inevitably are located in several different crystal field sites and random emission can happen from these different sites. Depending on the energy separation of these emissions and the resolving power of the detection system one may observe a series of fluorescence lines closely spaced and originated from ions in different crystal field sites.

In glass hosts where the number of different sites is very large, the fluorescence line under broad band excitation is very large, of the order of 100 cm^{-1}. If the active ion concentration is very low so that ion-ion interaction is not possible or energy migration does

not take place, then under laser excitation the fluorescence line is much narrower so that the inhomogeneous broadening is eliminated and only the homogeneous broadening caused by electron-phonon interactions is present. This type of study is usually referred to as "laser induced fluorescence line narrowing."

In crystal hosts where the number of different crystal field sites is much smaller than in glasses the laser induced fluorescence line narrowing leads to less spectacular results due to the fact that even in broad band excitation the fluorescence line is not very wide due to the small number of sites. In the event, though, that the emissions from the different crystal field sites are separated enough energy-wise for the resolving capabilities of the detection system, then the previously mentioned case of observing the individual transitions results. This case is at great interest because by exciting in different regions inside the Gaussian absorption line of ones interest, a selective excitation of the different sites associated with this absorption takes place. This process supplies one with more detailed information for interpreting energy transfer data and it is known as "site selection spectroscopy."

Introduction

For the reasons of interest in YVO_4 as a material of important optical applications, the previous chapter characterized the energy transfer from the host to the activator ions. A reasonable continuation of this work seems to be an attempt to characterize energy transfer between Eu^{3+} ions located in different YVO_4 field sites. Here the

Eu^{3+} ions are directly excited with a pulsed laser source whose bandwidth is much less than the width of the absorption transition and the fluorescence emission under these conditions can be resolved into a series of lines originating from ions in different crystal field sites. It is found that transfer takes place by electric dipole-dipole interaction whose characteristics are consistent with the properties of the spectral overlap integral. There is also strong indication of clustering of the europium ions.

Experimental

Samples and Equipment

A single crystal of yttrium orthovanadate doped with 1.0at% Eu^{3+} was obtained from Raytheon, Inc. The boule was grown along the crystallographic c-axis and a sample of about 5mm thickness was cut parallel to this direction.

The sample was mounted on the cold finger of a cryogenic refrigerator capable of continuously varying the temperature between about $7^{o}K$ and $300^{o}K$. Absorption measurements were made on a Cary 14 spectrophotometer. Fluorescence spectra and decay time measurements were obtained using the Systems Science and Software tunable dye laser pumped by the NRG pulsed nitrogen laser. The sample fluorescence is focused onto the entrance slit of the one-meter Czerny-Turner monochromater. The signal is detected by the cooled RCA C31034 photomultiplier tube, averaged by the boxcar integrator triggered by the nitrogen laser, and displayed on a strip chart recorder. The time resolution is about 0.5 μs.

Results

The dye laser was tuned to pump into one of the strong absorption lines of the $^7F_0$ - $^5D_2$ transition located at 4668.2Å as shown in Figure 18. Since the halfwidth of about 5.5 cm^{-1} of this line is an order of magnitude greater than the width of the laser, it is possible to selectively excite into different regions of the absorption line. The linewidth has contributions from both homogeneous broadening due to radiationless relaxation to the lower lying ^5D_J levels and from inhomogeneous broadening due to the presence of ions in slightly different crystal field sites. The latter effect allows for selective excitation of ions in specific sites by appropriately tuning the laser wavelength. The fluorescence transition from the $^5D_0$ metastable state to the lowest component of the $^7F_1$ level was monitored as the laser was tuned across the absorption line. The emission appeared as a series of several closely spaced sharp lines centered at about 5943Å. Three of these lines were significantly more intense than the others and their relative intensities vary as the excitation wavelength is changed as shown in Figure 18. These three lines have halfwidths of about 1.4 cm^{-1}. The middle and high energy lines are separated by 3.027 cm^{-1} and the middle and low energy lines by 4.754 cm^{-1}.

The fluorescence lifetimes of the three emission lines at 14°K are 472 μs for the high energy line, 527 μs for the middle line and 503 μs for the low energy line. At 122°K the lifetimes of these lines are 440 μs, 501 μs and 461 μs, respectively as shown in Table VIII.

To study energy transfer between trivalent europium ions in different crystal field sites, the fluorescence spectra of the three emission lines were obtained for different times after the laser pulse

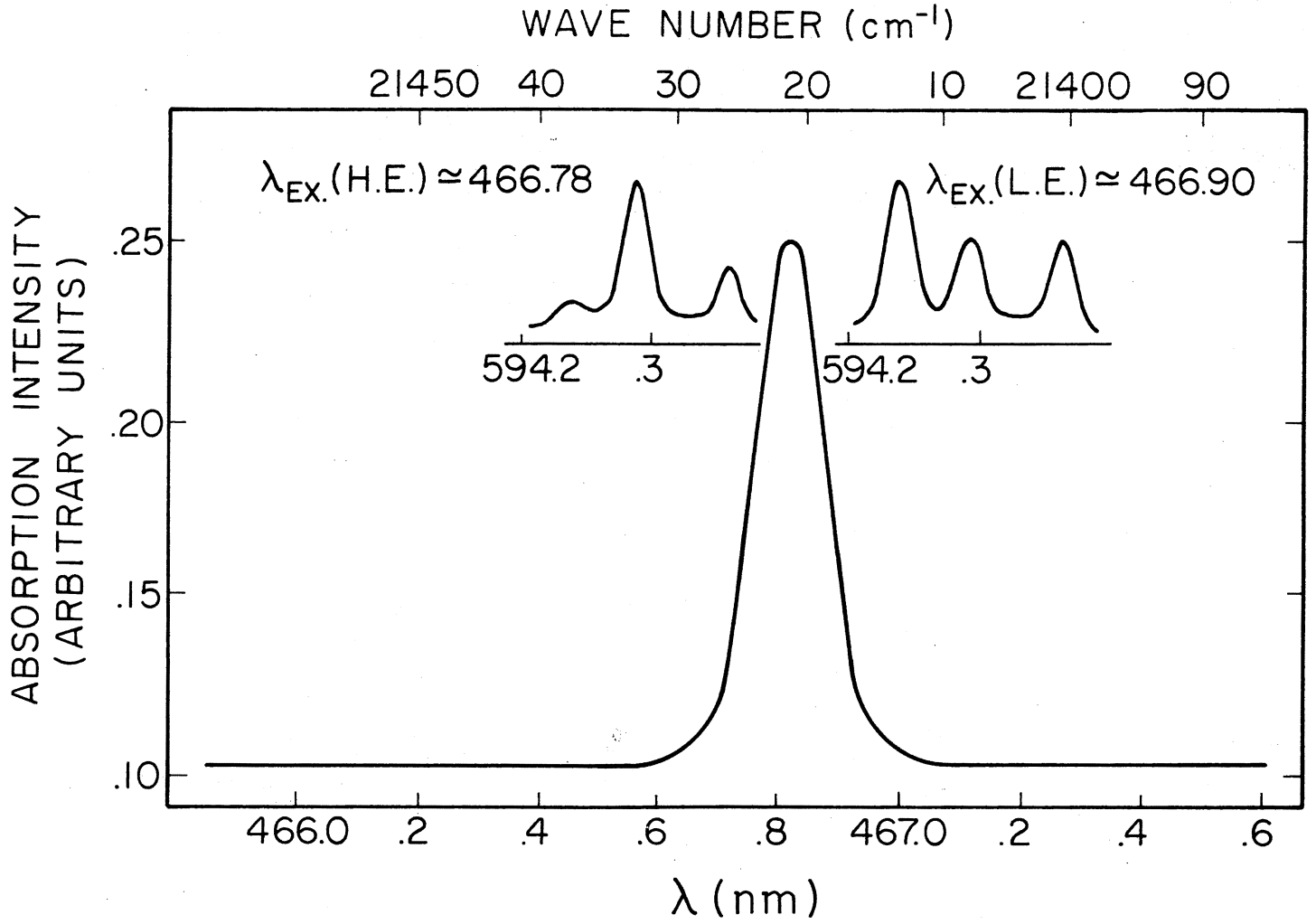

Figure 18. Absorption Line of the $^7F_0$-$^5D_2$ Transition of YVO_4:Eu^{3+}; Pumping at the High (H.E.) and Low (L.E.) Energy Side of This Line Produced Fluorescence Depicted on the Upper Two Scaled Down Diagrams

TABLE VIII

DECAY TIMES OF THE THREE Eu^{3+} EMISSION LINES

Temperature	High Energy Line	Middle Energy Line	Low Energy Line
$14^{o}K$	472 μs	527 μs	503 μs
$122^{o}K$	440 μs	501 μs	461 μs

These time-resolved spectroscopy (TRS) results were then analyzed by finding the integrated fluorescence intensities at each time. Figure 19 (and Table IX) shows the ratios of the intensities of the high and low energy emission lines to that of the middle line as a function of time after the laser pulse for high energy excitation (4667.8Å) at 11°K. Similar TRS results are shown in Figure 20 for low energy excitation (4669.0Å) at 11°K. In this case the ratios of the intensities of each line to the total intensity of the three lines are plotted versus time.

For other settings of the excitation wavelength a variety of different time dependences can be obtained for the fluorescence intensity ratios. Similar measurements were made at numerous temperatures up to 138°K and only a small change in intensity ratios was observed with temperature as shown in Figure 21.

Interpretation

The TRS data shown in Figure 19 for high energy excitation indicate that in this case the ions in sites giving rise to the middle line are selectively excited and energy is transferred to the ions in the other types of sites responsible for the higher and lower energy lines. A quantitative interpretation of these data can be obtained using the model shown in Figure 22. The excited state populations are designated as n_L, n_M, and n_H for the low, middle and high levels, respectively. The direct pumping rates of these levels are W_L, W_M, and W_H while their intrinsic decay rates are B_L, B_M and B_H. $P_{MH}(t)$ and $P_{ML}(t)$ are the energy transfer rates which may be functions of time. The rate equations for the excited state populations are

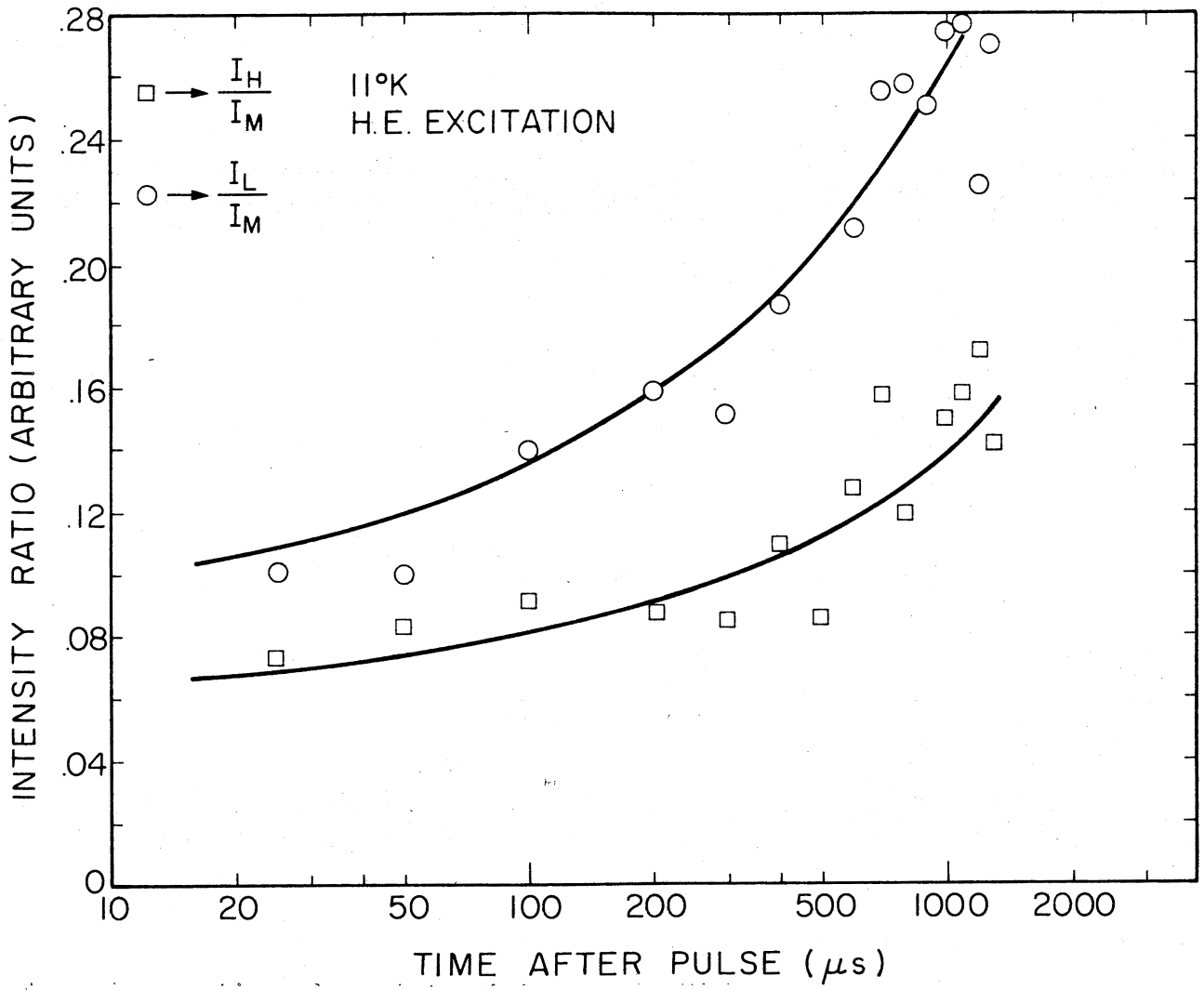

Figure 19. Ratios of the Intensities of the High (I_H) and Low (I_L) Energy Emission Lines to That of the Middle Line or a Function of Time After the Laser Pulse for 4667.8A Excitation at 11°K

TABLE IX

FLUORESCENCE INTENSITY RATIOS FOR HIGH ENERGY EXCITATION MEASURED AT DIFFERENT TIMES AFTER PULSE (FIGURE 19)

μs After Pulsa	I_{H/I_M}	I_{L/I_M}
25	.074	.103
50	.084	.100
100	.092	.140
200	.088	.160
300	.085	.152
400	.110	.187
500	--	--
600	.128	.212
700	.159	.256
800	.120	.258
900	.153	.251
1000	.150	.275
1100	.158	.277
1200	.172	.225
1300	.142	.270

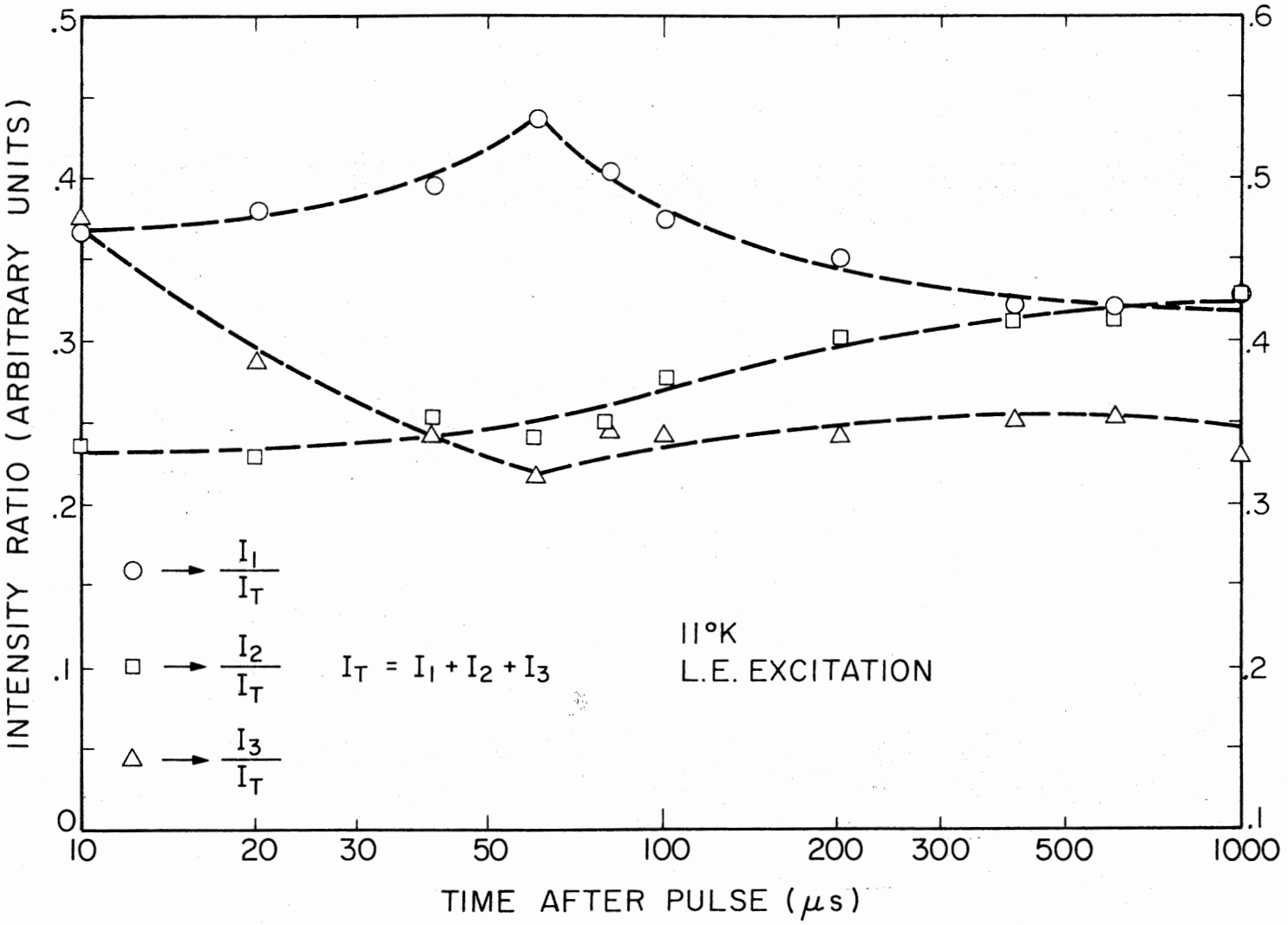

Figure 20. Ratios of the Intensities of High (I_H), Middle (I_M) and Low (I_L) Energy Emission Lines, to the Sum of the Three Intensities as a Function of Time After the Laser Pulse for 4669.0Å Excitation at 11°K

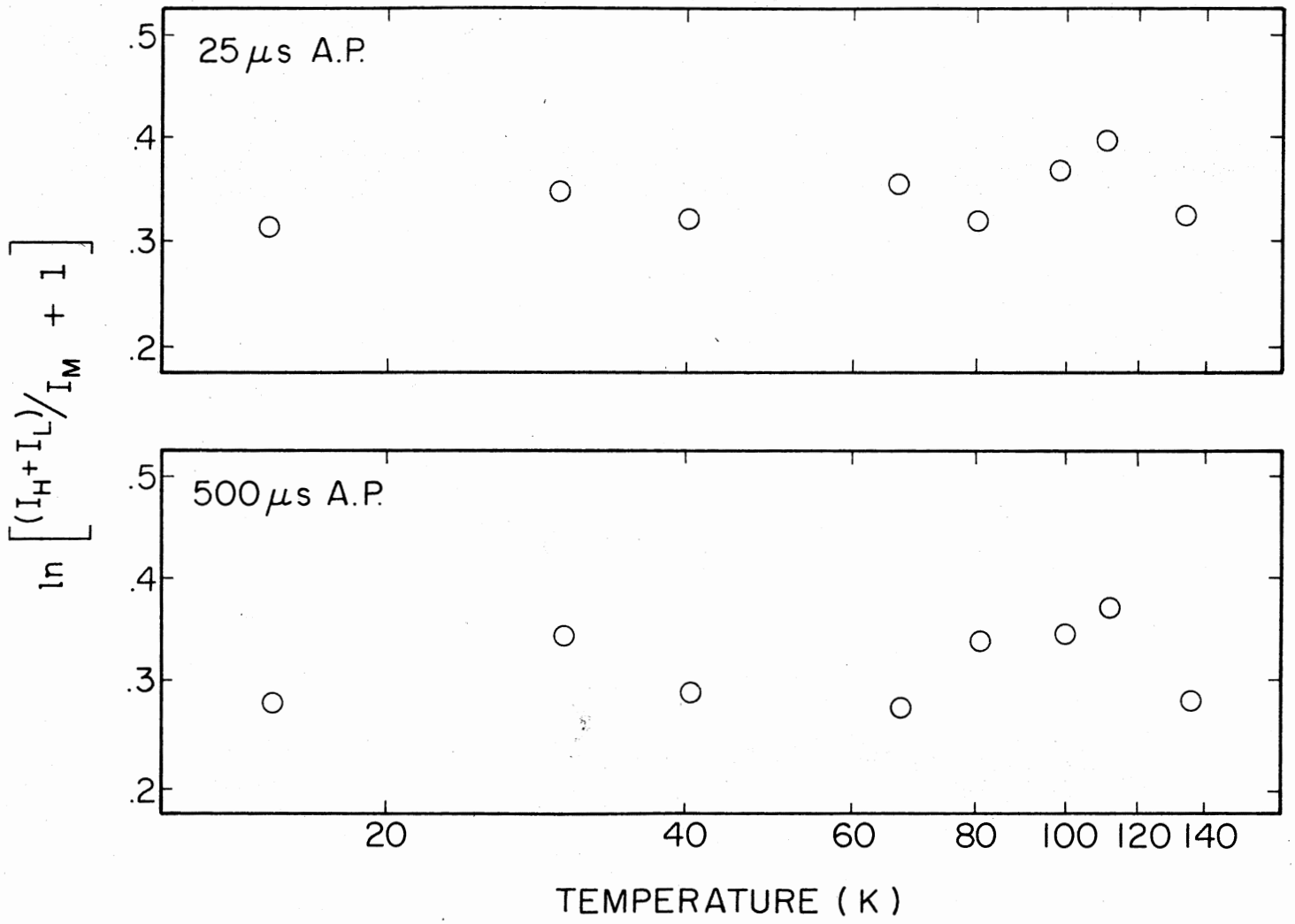

Figure 21. Temperature Dependence of the Intensity Ratios Taken at 25 and 500 μs After the Laser Pulse

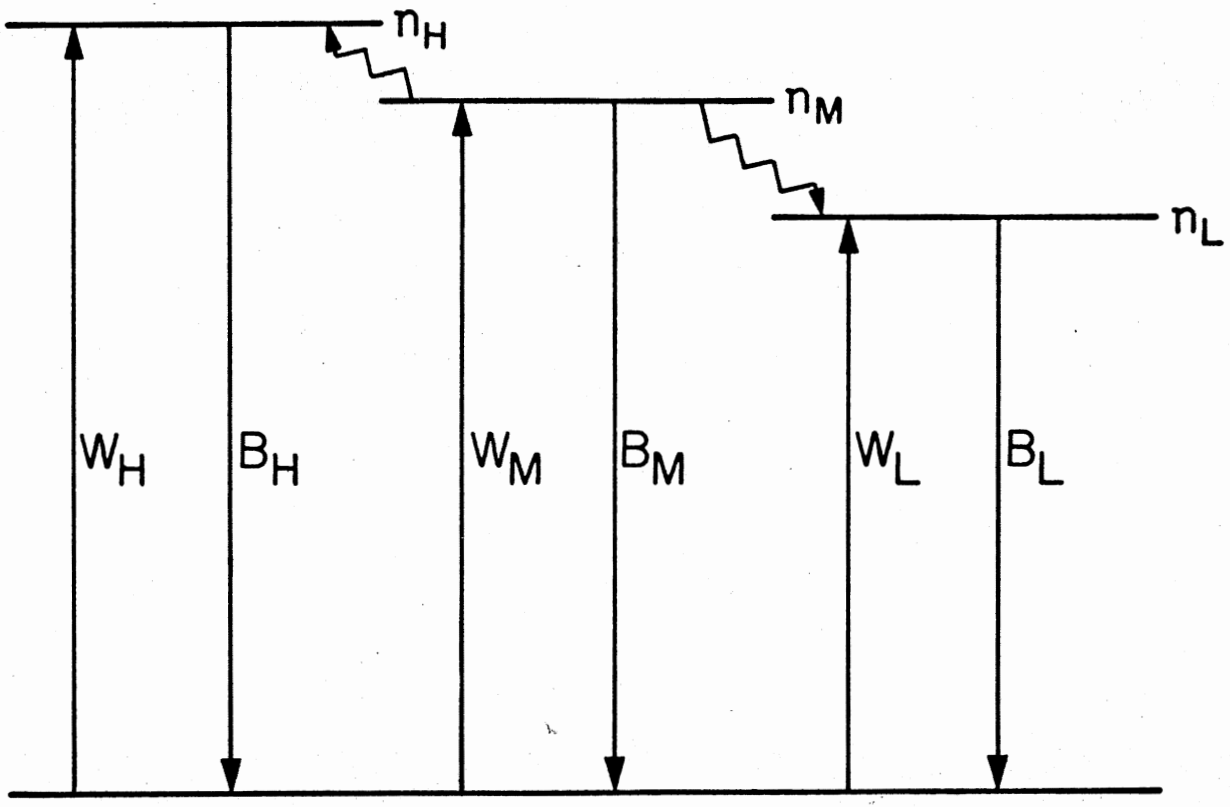

Figure 22. Model Used for Interpreting the Site Selection Spectroscopy Results for $YVO_4:Eu^{3+}$

$$dn_M/dt = W_M - B_M n_M - (P_{MH} + P_M) n_M \quad (3\text{-}1)$$

$$dn_H/dt = W_H - B_H n_H + P_{MH} n_M \quad (3\text{-}2)$$

$$dn_L/dt = W_L - B_L n_L + P_{ML} n_M \quad . \quad (3\text{-}3)$$

These can be solved assuming delta function excitation and the observed fluorescence intensities are proportional to these populations. If the small differences in fluorescence lifetimes and radiative decay rates for the three lines are neglected, the resulting fluorescence intensity ratios are predicted to be

$$I_H/I_M = \left\{\left[(I_H(o)/I_M(o) + P_{MH}/(P_{MH}+P_{ML})\right] \exp\left[(P_{MH}+P_{ML})t\right] - P_{MH}/(P_{MH}+P_{ML})\right\} \quad (3\text{-}4)$$

$$I_L/I_M = \left\{\left[(I_L(o)/I_M(o)) + P_{ML}/(P_{MH}+P_{ML})\right] \exp\left[(P_{MH}+P_{ML})t\right] - P_{ML}/(P_{MH}+P_{ML})\right\} \quad (3\text{-}5)$$

$$(I_H+I_L)/I_M = \left[(I_H(o)+I_L(o)/I_M(o) + 1\right] \exp\left[(P_{MH}+P_{ML})t\right] - 1 \quad (3\text{-}6)$$

Equations (3-4) through (3-6) can be fit to the TRS data in Figure 19 by treating P_{MH} and P_{ML} as adjustable parameters and the results are shown as the solid lines in the figure. The procedure for doing this was to first plot the ratio $(I_H+I_L)/I_M$ on a semilog scale versus time to different powers in order to determine the time dependence of the energy transfer. The energy transfer rate for a single step process

between randomly distributed sensitizers and activators is given by (10)

$$P_{SA} = \Gamma(1-3/q)\frac{4}{3}\pi R_o^3 C_A (t/\tau)^{3/q} t^{-1} \qquad (3\text{-}7)$$

where q=6, 8, or 10 for electric dipole-dipole, dipole-quadrupole and quadrupole-quadrupole interactions, respectively, R_o is the critical interaction distance and C_A is the activator concentration. In this case the results are consistent with a $t^{1/2}$ time dependence with $P_{MH}+P_{ML} = 6.35 \times 10^{-3}\ \mu s^{-1/2}$. These results were used in Eqs. (3-4) and (3-5) to fit the I_H/I_M and I_L/I_M curves of Figure 19. This gives $P_{MH} = 4.49 \times 10^{-3}\ \mu s^{-1/2}$ and $P_{ML} = 1.86 \times 10^{-3}\ \mu s^{-1/2}$.

The values for the critical energy transfer distances can be found from substituting the measured values of the energy transfer rates into Eq. (3-7). To do this it is necessary to know the value of the activator ion concentration which means in this case knowing the number of Eu^{3+} ions in each different kind of site. Although this is difficult to determine accurately, a reasonably good estimate can be obtained by comparing the relative intensities of the three lines normalized to the total emission for all excitation wavelengths across the absorption line at short times after the laser pulse. Then the maximum intensity of each line adjusted to account for differences in total excitation energy, is taken to be an indication of the concentration of europium ions in the type of site giving rise to the line. The results indicate that 0.280 of the Eu^{3+} ions are in the type of sites giving the high energy emission line; 0.573 of the ions are in the sites having the middle energy emission line; and 0.147 of the ions are in the low energy sites. Using these number in Eq. (3-7) gives

values of $R_o(MH) = 8.85\mathring{A}$ and $R_o(ML) = 8.18\mathring{A}$. A theoretical estimate for R_o can be obtained from the expression

$$R_o = \left[\frac{3}{4}\frac{n_s}{(2\pi n\bar{\nu}_{SA})^4}\left(\frac{e^2}{mc^2}\right) f_A\, \Omega\right]^{1/6} \qquad (3\text{-}8)$$

where n_s is the quantum efficiency of the sensitizer, Ω is the overlap integral of the absorption spectrum of the activator and the emission spectrum of the sensitizer, n is the index of refraction, $\bar{\nu}_{SA}$ is the average wavenumber in the region of spectral overlap, and f is the oscillator strength of the activator given by:

$$f_A = \frac{mc}{8\pi^2 e^2 \bar{\nu}_{SA}^2}\,. \qquad (3\text{-}9)$$

To accurately determine R_o from this expression it would be necessary to observe transitions from the $^5D_0$ level to the ground state in both absorption and emission. Since these are forbidden transitions and thus very weak it is difficult to observe them accurately with the required resolution to separate the lines from ions in different sites. However, if it is assumed that the line positions and shapes are determined primarily by the $^5D_0$ level, the fluorescence spectra such as those shown in Figure 1 can be used to determine spectral overlap. This can be done using the expression for the convolution integral of two overlapping Lorentzion line shape function

$$\Omega = \int g_S(\omega) g_A(\omega) d_\omega = \frac{1}{\pi}\,\frac{\Delta\omega_S + \Delta\omega_A}{(\Delta\omega_S+\Delta\omega_A)^2 + (\omega_S^o - \omega_A^o)^2} \qquad (3\text{-}10)$$

In this case it is found that $\Omega_{(MH)} = 0.0558\ cm^{-1}$ and $\Omega_{(ML)} = 0.0255\ cm^{-1}$ and these values substituted into Equation (3-8) give $R_o(MH) = 24.9\mathring{A}$

and $R_o(ML) = 26.2\text{Å}$. These values of the theoretically predicted critical interaction distance are obtained under the assumptions that the Eu^{3+} ions are uniformly distributed in the YVO_4 crystal and that the measured fluorescence lines are narrowed down to their homogeneous line width. These values of R_o therefore constitute an upper limit. But due to instrument limitations the fluorescence lines are not narrowed down completely and inhomogeneous broadening is still present. It has been shown by Yen and coworkers (11) that these lines can be narrowed down by orders of magnitude and by using these values for line width we obtain minimum spectral overlap values smaller by six orders of magnitude. This leads to lower limit values of R_o in the neighborhood of 3Å. It appears also that in reality the Eu^{3+} ions are not uniformly distributed but they form clusters with an average separation between 3Å and 25Å within the cluster.

The more complex TRS results obtained for low energy excitation shown in Figure 20 are more difficult to interpret quantitatively. It appears that the low energy site is preferentially excited and between 10 and 60 μs after the excitation pulse energy is being transferred to ions in the middle and high energy sites. The amount of decrease in the I_L/I_T ratio between 20 and 60 μs is exactly the same as the amount of increase in the sum of the I_H/I_T and I_M/I_T ratios in this region. The ratio of the high energy line increases about 4.8 times more than the ratio of the middle energy line indicating that transfer to ions in the high energy site is dominant. Between 60 and 600 μs it appears that energy is transferred from ions in the high energy site to those in the middle and low energy sites. The decrease in the I_H/I_T ratio is

the same as the sum of the increases in the middle and low energy intensity ratios in this time region with the middle energy line increasing about 1.9 times more than the low energy line. These complicated interactions of transfer and back transfer among the ions in the three types of sites and their variations with time make it impossible to quantitatively fit the data with any simple rate equation model.

Discussion

The results described above indicate that there are three major types of crystal field sites for Eu^{3+} ions to occupy in YVO_4 crystals and that energy transfer takes place among the ions in these different types of sites by a single step, electric dipole-dipole interaction process. The values of the critical interaction distances of the order of 8Å are much smaller than the average separation uniformly distributed europium ions of 25Å in a sample containing 1.0% Eu^{3+}. This indicates that the europium ions in different sites are tending to form clusters.

The Eu^{3+} ions substitute for the Y^{3+} ions in yttrium orthovanadate and are in a site of D_{2d} symmetry with ten vanadate sites and four other yttrium sites within 5Å away. There are two equivalent types of sites related by a 90^{o} rotation about the c-axis. The ionic radius of Eu^{3+} is 1.03Å which is somewhat larger than the 0.93Å radius of Y^{3+}. From previous studies of host sensitized energy transfer in this material it is known that Eu^{3+} impurity ions create local distortions in the neighboring VO_4^{3-} complexes (12) (13). These local distortions may be different in the two types of yttrium sites making them nonequivalent. Also having nearby europium ions due to clustering can give rise to

different nonequivalent sites. Finally, one of the major problems of yttrium orthovanadate crystals is the presence of imperfections introduced during crystal growth (14). If a chemical or structural imperfection is located near to the Eu^{3+} ion different types of sites could result. Thus there are several possible origins for the different types of crystal field sites for Eu^{3+}. There has been some previous evidence for different types of sites of Nd^{3+} in YVO_4 at higher concentrations which is not observed at lower concentrations (15). This may again indicate clustering is important. However, in the Nd^{3+} case the energy difference between sites is several hundred wavenumbers as compared to the very small splitting of only a few wavenumbers observed here for Eu^{3+}.

There has recently been a significant amount of interest in characterizing the dependence of energy transfer rates on the differences in transition energies of the sensitizer and activator ions and on temperature (11) (16) (17) (2) (3). This interest is derived from the fact that the use of high resolution laser excitation allows the study of energy transfer between ions whose energy mismatch is so small that the density of single phonons available to conserve energy is negligible, and thus the usual treatments of phonon assisted energy transfer do not apply. Because of this, Holstein and coworkers (2) (3) have developed theories of two-phonon assisted energy transfer which show that the different types of possible two-phonon processes give rise to a variety of dependences on temperature and energy mismatch. For the results obtained on Eu^{3+} ions with high energy excitation the energy transfer rates to the high and low energy lines from the middle line are approximately proportional to $1/\Delta E^2$ where ΔE is the energy

difference between the middle line and either the high or low energy lines. The temperature dependence of the transfer rates for this case is very weak, approximately proportional to the homogeneous linebroadening. These results are consistent with standard resonant energy transfer theory where the temperature and energy mismatch dependences are contained in the spectral overlap factor as given by Eq. (3-10). If the linewidths $\Delta\omega$ are small compared to the line splittings ΔE, this predicts $P_{SA} \propto \Delta\omega/\Delta E^2$. Although this is only marginally true in this case, this simple theory appears to give the most satisfactory description of the observed results. The more complicated two-phonon theories can predict the observed dependences on energy mismatch but they generally predict much stronger temperature dependences (2). The only type of process discussed by Holstein et al. (2) which might give the observed weak temperature dependence is the two-phonon process involving resonant interaction with a real intermediate electronic state. For the case of Eu^{3+} emission from the $^5D_0$ level and transfer to an ion in the $^7F_0$ ground state, this process will be negligible since the energy separations to the closest electronic levels in both the ground and excited states are quite large compared to kT. Orbach (18) has pointed out that the spectral overlap approach is valid for this situation if in addition the energy mismatch and the linewidths are much less than kT. All of these criteria are met in the case discussed here. Also if the transfer occurs between europium ions only 8Å apart as concluded above the long wave length phonon approximation will be valid and such things as phonon interference factors can be neglected.

These results are consistent with a similar study made earlier on energy transfer between Sm^{3+} ions in $CaWO_4$ crystals where spectral overlap consideration also gave a satisfactory description of the results. In both of these cases the differences in transition energies for ions in nonequivalent crystal field sites are great enough to allow the emission of lines from ions in different sites to be distinctly resolved. In other cases where transfer occurs to an ensemble of different sites quasicontinuously distributed in energy, it has been found necessary to interpret the data using the more complex two-phonon assisted theories of the Introductory chapter. These two different physical cases may indicate the region of validity of the spectral overlap method for accounting for phonons in energy transfer processes.

CHAPTER IV

SUMMARY AND CONCLUSIONS

The Host-Sensitized $YVO_4:Eu^{3+}$ and $YVO_4:Er^{3+}$ Systems

In summary, host-sensitized energy transfer in yttrium vanadate crystals doped with trivalent rare earth impurity ions at low temperatures is consistent with a single step electric dipole-dipole interaction process from self-trapped excitons, whereas at high temperatures the transfer is dominated by thermally activated exciton hopping with activator induced host traps having an important part in the trapping process. In the latter case both the hopping steps and the trapping steps appear to be due to exchange interaction. This is consistent with the fact that the charge distribution of the $^1A_1$ metastable state of the vanadate molecule lies outside the molecule, thus providing for the possibility of strong wave function overlap with neighboring vanadate molecules and impurity ions (19). Since exchange interaction falls off rapidly with distance, it is not surprising that at low temperatures where the excitons are immobile, longer range electric dipole-dipole interaction processes become important.

The transition models and rate equations used in interpreting the $YVO_4:Eu^{3+}$ and $YVO_4:Er^{3+}$ data are fairly complex. However, it should be reiterated that many simpler models were investigated and found to

be unacceptable for fitting the data. The complexity due to the activator-induced host traps should be expected since similar defect sites are necessary for explaining the data obtained on undoped YVO_4. In this case the perturbing defects are structural imperfections or chemical impurities other than activator ions.

A final important point to note is that pulsed laser TRS measurements produced data which are consistent with conventional lifetime and intensity quenching studies but is more sensitive to the choice of models used in interpretation of the results. This leads directly to more primary experimental parameters, thus alleviating the necessity for many of the assumptions that generally must be made in obtaining migration and trapping characteristics from primary experimental parameters. This is especially important in cases where many different interaction and relaxation processes are present such as the systems investigated here.

Site Selection Spectroscopy of Eu^{3+} in $YVO_4:Eu^{3+}$

In conclusion, high resolution, laser time-resolved site selection spectroscopy has been shown to give useful information on the characteristics of energy transfer between europium ions in yttrium orthovanadate crystals. The Eu^{3+} ions are shown to occupy several different types of crystal field sites and are probably in clusters. The energy transfer mechanism is electric dipole-dipole interaction and the transfer takes place over distances of the order of 8Å. The characteristics of the energy transfer can be successfully explained using a resonant interaction theory and the properties of spectral overlap. The

characteristics of the fluorescence emisson and energy transfer are critically dependent on the exact wavelength of excitation and in some cases the results are too complicated to interpret through a simple rate equation approach. In these cases it is necessary to develop a computer fitting of the data which includes all of the different types of interactions taking place (3). Finally, it should be noted that information on active ion site distributions and interactions such as obtained here is useful in understanding the properties of rare earth doped yttrium orthovanadate as it is used for phosphors, lasers and other optical applications.

Conclusions

This study demonstrates the usefulness of dye laser time-resolved spectroscopy and site selection spectroscopy in obtaining detailed information on energy transfer in systems like the rare earth ions in phosphors. In this type of system great parts of the energy transfer mechanisms remain hidden under examination with conventional spectroscopy techniques. One would think that a computer fitting of the data that was mentioned previously could give some more information, as well as an examination with higher resolution lasers. Finally, an investigation of the same host crystal with different impurity ions using site selection spectroscopy techniques seems to be a natural continuation in the effort of understanding the different energy transfer processes.

REFERENCES

1. Yokota, M. and O. Tanimoto, J. Phys. Soc. Japan 22, 779 (1967).

2. Holstein, T., S. K. Lyo, and R. Orbach, Phys. Rev. Letters 36, 891 (1976).

3. Holstein, T., S. K. Lyo, and R. Orbach, Phys. Rev. (to be published). A preliminary account of this work was presented at the Colloque International du C.N.R.S. "Spectrocopie des Elements Transitions et des Elements Lourds dan les Solides," 1976.

4. Hsu, C. and R. C. Powell, J. Luminescence 10, 273 (1975).

5. Reed, E. D. and H. W. Moos, Phys. Rev. B 8, 980 (1973).

6. DiBartolo, B., Boston College Report for the U. S. Air Force, Unpublished.

7. Soos, Z. G. and R. C. Powell, Phys. Rev. B 6, 4035 (1972).

8. Ozawa, L. and H. N. Hersh, Phys. Rev. Letters 36, 683 (1976).

9. Powell, R. C. and Soos, Z. G., J. Luminescence 11, 1 (1975).

10. Inokuti, M. and F. Hirayama, J. Chem. Phys. 43, 1978 (1965).

11. Flach, R., D. S. Hamilton, P. S. Selzer, and W. M. Yen, Phys. Rev. Letters 35, 1034 (1975); Phys. Rev. B15, 1248 (1977).

12. Hsu, C. and R. C. Powell, J. Luminescence 10, 273 (1975).

13. Venikouas, G. E. and R. C. Powell, J. Luminescence (to be published).

14. Yaney, P. P. and L. G. DeShazer, J. Opt. Soc. America 66, 1405 (1976).

15. Bagdasarov, Kh. S., G. A. Bogomolova, A. A. Kaminskii, and V. I. Popov, Soviet Physics Doklady 13, 516 (1968).

16. Hsu, C. and R. C. Powell, Phys. Rev. Letters 35, 734 (1975); J. Phys. C9, 2467 (1976).

17. Selzer, P. M., D. S. Hamilton, and W. M. Yen, Phys. Rev. Letters 38, 858 (1977).

18. Orbach, private communication.

19. Boudreaux, D. S. and T. S. LaFrance, J. Phys. Chem. Solids 35, 897 (1974).

VITA[2]

George Venikouas

Candidate for the Degree of

Doctor of Philosophy

Thesis: LASER SPECTROSCOPY STUDIES OF ENERGY TRANSFER IN $YVO_4:Eu^{3+}$, Er^{3+}

Major Field: Physics

Biographical:

Personal Data: Born in Athens, Greece, April 22, 1945.

Education: Attended elementary schools in Athens, Greece, and was graduated from high school there in 1963. Attended University of Thessaloniki in Thessaloniki, Greece, from 1964 to 1970 and received a Bachelor degree in June of 1970. Spent two and a quarter years in the Army Signal Corps and left as a Second Lieutenant. Entered graduate school in physics at Oklahoma State University in the Fall of 1973 and completed requirements for Doctor of Philosophy degree in May, 1978.